

Bézier \bar{B} projection

Di Miao^{1,*} Michael J. Borden¹ Michael A. Scott¹ Derek C. Thomas²

¹Department of Civil and Environmental Engineering
Brigham Young University
368 CB, Provo, UT 84602, USA

²Coreform LLC
P.O. Box 970336, Orem, UT 84097, USA

In this paper we demonstrate the use of Bézier projection to alleviate locking phenomena in structural mechanics applications of isogeometric analysis. Interpreting the well-known \bar{B} projection in two different ways we develop two formulations for locking problems in beams and nearly incompressible elastic solids. One formulation leads to a sparse symmetric system and the other leads to a sparse non-symmetric system. To demonstrate the utility of Bézier projection for both geometry and material locking phenomena we focus on transverse shear locking in Timoshenko beams and volumetric locking in nearly compressible linear elasticity although the approach can be applied generally to other types of locking phenomena as well. Bézier projection is a local projection technique with optimal approximation properties, which in many cases produces solutions that are comparable to global L^2 projection. In the context of \bar{B} methods, the use of Bézier projection produces sparse stiffness matrices with only a slight increase in bandwidth when compared to standard displacement-based methods. Of particular importance is that the approach is applicable to any spline representation that can be written in Bézier form like NURBS, T-splines, LR-splines, etc. We discuss in detail how to integrate this approach into an existing finite element framework with minimal disruption through the use of Bézier extraction operators and a newly introduced dual basis for the Bézier projection operator. We then demonstrate the behavior of the two proposed formulations through several challenging benchmark problems.

Keywords: Isogeometric analysis, Bézier extraction, Bézier dual basis, Bézier projection, \bar{B} -projection, locking

1 Introduction

Isogeometric analysis (IGA), introduced by Hughes et al. [1], adopts the spline basis, which underlies the CAD geometry, as the basis for analysis. Of particular importance is the positive impact of smoothness on numerical solutions, where, in many application domains, IGA outperforms classical finite elements [2–7]. Initial investigations of IGA focused on non-uniform rational B-splines (NURBS) due to their dominance in commercial CAD packages. However, many advances are being made in analysis-suitable geometry representations that overcome the strict rectangular topological restrictions of NURBS. Examples include T-splines [6, 8] and their analysis-suitable restriction [9, 10], hierarchical B-splines [11–15], and locally refined B-splines [16, 17] among others.

The purpose of this paper is to demonstrate how Bézier projection [18] can be employed as the underlying local projection framework for a \bar{B} approach to treat locking in isogeometric structural elements. Bézier projection is an element-based local projection methodology for B-splines, NURBS, and T-splines. It relies on the concept of Bézier extraction [19, 20] and an associated operation, spline reconstruction, which enables the use of Bézier projection in standard finite element codes.

Bézier projection exhibits provably optimal convergence and yields projections that are virtually indistinguishable from global L^2 projection. For an isogeometric finite element code that leverages Bézier extraction, Bézier projection can be employed virtually for free. To simplify the implementation of the Bézier \bar{B} method in existing finite element codes we develop a *dual* element Bézier extraction operator that can be derived directly from the Bézier extraction of a spline representation. It is worth noting that Bézier projection can also be used to develop a unified framework for spline operations including cell subdivision and merging, degree elevation and reduction, basis roughening and smoothing, and spline reparameterization and is applicable to any spline representation that can be written in Bézier form.

Numerical locking in structural finite elements includes geometric locking in thin curved structural members such as membrane and shear locking and also includes volumetric locking in incompressible and nearly incom-

*miaodi1987@gmail.com

pressible elasticity. There is an immense body of literature on approaches to overcome locking in the finite element community and various approaches have emerged as dominant. These include reduced quadrature [21,22], \bar{B} projection methods [23–25], and mixed methods based on the Hu-Washizu variational principle [26–29]. It is important to mention that, although ameliorated at high polynomial degrees, smooth splines in the context of IGA still exhibit locking behavior [30,31].

In IGA, there is a growing literature on the treatment of locking in structural elements. Leveraging higher-order smoothness, transverse shear locking can be eliminated at the theoretical level by employing Kirchhoff-Love [32,33] and hierarchic Reissner-Mindlin [34–36] shell elements. Reduced quadrature schemes have been explored in [37–39] as a way to alleviate transverse shear locking. The extension of \bar{B} projection to the isogeometric setting was initiated in [40] for both elastic and plastic problems and was extended in [41] to include local projection techniques [42,43].

In this paper we introduce two methods that employ Bézier projection to produce a localized approximation to the standard \bar{B} method. The motivation behind these methods is the fact that \bar{B} methods result in dense linear systems. The methods we introduce result in a sparse linear system irrespective of the choice of basis functions. We call these two methods the symmetric and non-symmetric Bézier \bar{B} projection methods, where the names indicate the symmetry of the resulting stiffness matrix. We show that both methods result in a sparse stiffness matrix and reduce locking. We also show that optimal convergence rates are achieved in the case of the non-symmetric method and near optimal convergence rates are achieved in the case of the symmetric method. We also perform an inf-sup analysis of these methods.

The outline of this paper is as follows: First, we briefly review spline basis functions in Section 2. In Sections 3 and 4, we describe Bézier extraction and projection. We then formulate and use Bézier \bar{B} projection for the Timoshenko beam (to treat transverse shear locking) and nearly incompressible elasticity (to treat volumetric locking) in Sections 5 and 6, respectively. We provide detailed element level operations in both settings. We also presents numerical tests to show the performance of the proposed strategy.

2 Preliminaries and notation

In this section a brief overview of univariate Bernstein, B-spline, and NURBS basis functions is provided. We also describe how these univariate basis functions are extended to higher dimensions.

2.1 Univariate Bernstein basis functions

The i th univariate Bernstein basis function of degree p is defined by

$$B_{i,p}(\xi) = \binom{p}{i} \xi^i (1 - \xi)^{p-i} \quad (1)$$

where $\xi \in [0, 1]$ and $\binom{p}{i} = \frac{p!}{i!(p-i)!}$, $0 \leq i \leq p$, is a binomial coefficient.

2.2 Univariate spline basis functions

A univariate B-spline basis of dimension n is defined by a polynomial degree p and a knot vector $\Xi = \{\xi_0, \xi_1, \dots, \xi_{n+p}\}$, which is a non-decreasing sequence of real numbers. The A th B-spline basis function can then be defined using the Cox-de Boor recursion formula:

$$N_{A,0}(\xi) = \begin{cases} 1 & \xi_A \leq \xi \leq \xi_{A+1} \\ 0 & \text{otherwise} \end{cases} \quad (2)$$

$$N_{A,p}(\xi) = \frac{\xi - \xi_A}{\xi_{A+p} - \xi_A} N_{A,p-1}(\xi) + \frac{\xi_{A+p+1} - \xi}{\xi_{A+p+1} - \xi_{A+1}} N_{A+1,p-1}(\xi). \quad (3)$$

For simplicity, we will always use open knot vectors defined over the interval $[0, 1]$. An open knot vector satisfies the conditions $\xi_0 = \xi_1 = \dots = \xi_p = 0$ and $\xi_n = \xi_{n+1} = \dots = \xi_{n+p} = 1$ and creates interpolatory end conditions. B-spline basis functions can be used to represent piecewise polynomial functions but are not capable of representing conic sections (e.g. circles, ellipses and hyperbolas). NURBS overcome this shortcoming. A NURBS basis function can be written as

$$R_{A,p}(\xi) = \frac{N_{A,p}(\xi)w_A}{W(\xi)} \quad (4)$$

where w_A is called a weight and

$$W(\xi) = \sum_A N_{A,p}(\xi) w_A \quad (5)$$

is called the weight function. A d -dimensional rational curve $\mathbf{S}(\xi) \in \mathbb{R}^d$ can then be defined as

$$\mathbf{S}(\xi) = \sum_A R_{A,p}(\xi) \mathbf{P}_A \quad (6)$$

where $\mathbf{P}_A = (p_A^1, p_A^2, \dots, p_A^d)^T$ is a d -dimensional control point. It is often more convenient to represent the d -dimensional NURBS in a $(d+1)$ -dimensional homogeneous space by defining $\mathbf{P}_A^w = (p_A^1 w_A, p_A^2 w_A, \dots, p_A^d w_A, w_A)^T$ and the corresponding $(d+1)$ -dimensional B-spline curve as

$$\mathbf{S}^w(\xi) = \sum_A N_{A,p}(\xi) \mathbf{P}_A^w \quad (7)$$

such that each component of \mathbf{S}^w can be written as

$$S_i(\xi) = \frac{S_i^w(\xi)}{S_{d+1}^w(\xi)}. \quad (8)$$

In the homogeneous form, NURBS can be manipulated with standard B-spline algorithms.

2.3 Multivariate spline basis functions

In higher dimensions, Bernstein, B-spline, and NURBS basis functions are formed by the Kronecker product of univariate basis functions. For example, two-dimensional B-spline basis functions of degree $\mathbf{p} = (p_\xi, p_\eta)$ are defined by

$$\mathbf{N}^{\mathbf{p}}(\xi, \eta) = \mathbf{N}^{p_\xi}(\xi) \otimes \mathbf{N}^{p_\eta}(\eta) \quad (9)$$

where $\mathbf{N}^{p_\xi}(\xi)$ and $\mathbf{N}^{p_\eta}(\eta)$ are vectors of basis functions in the ξ and η directions, respectively. A particular multivariate basis function can be written as

$$N_{A(i,j)}^{\mathbf{p}}(\xi, \eta) = N_{i,p_\xi}(\xi) N_{j,p_\eta}(\eta) \quad (10)$$

where the index mapping is defined as

$$A(i, j) = n_\eta i + j. \quad (11)$$

The integer n_η is the number of basis functions in η direction.

3 Bézier extraction

Given a spline basis \mathbf{N} there exists a Bernstein basis \mathbf{B} and a linear operator \mathbf{C} (see [19]) such that

$$\mathbf{N}(\xi) = \mathbf{C}\mathbf{B}(\xi). \quad (12)$$

The localization of \mathbf{C} to an element domain produces the element extraction operator \mathbf{C}^e . Given control points \mathbf{P}^e , the corresponding Bézier control points \mathbf{Q}^e can be computed directly as

$$\mathbf{Q}^e = (\mathbf{C}^e)^T \mathbf{P}^e. \quad (13)$$

A graphical depiction of Bézier extraction is shown in Figure 1.

4 Bézier projection

Bézier projection can be viewed as the inverse of extraction [18]. Bézier projection uses an element reconstruction operator $\mathbf{R}^e \equiv (\mathbf{C}^e)^{-1}$ such that the global control point values, corresponding to those basis functions defined over the support of an element e , can be determined directly from Bézier control values as

$$\mathbf{P}^e = (\mathbf{R}^e)^T \mathbf{Q}^e \quad (14)$$

where \mathbf{Q}^e is any field in Bézier form. The action of the element reconstruction operator is depicted graphically in Figure 1. For example, given any function $u \in L^2$, we can compute \mathbf{Q}^e as

$$\mathbf{Q}^e = (\mathbf{G}^e)^{-1} \mathbf{F}^e \quad (15)$$

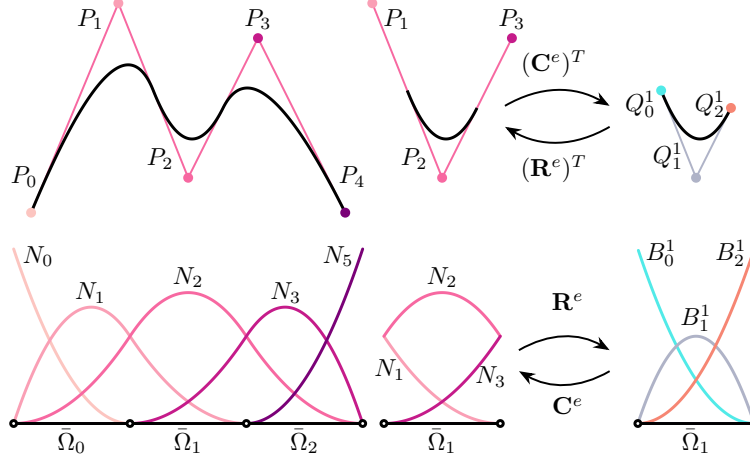


Figure 1: Illustration of Bézier extraction and projection in one dimension for a B-spline of degree 2 and knot vector $[0, 0, 0, 1/3, 2/3, 1, 1, 1]$ (restricted to the second element for illustrative purposes).

where \mathbf{G}^e is the Gramian matrix corresponding to the Bernstein basis with components

$$G_{ij}^e = \int_{\Omega^e} B_i^e B_j^e d\Omega = \langle B_i^e, B_j^e \rangle_{\Omega^e} \quad (16)$$

and

$$F_i^e = \int_{\Omega^e} B_i^e u d\Omega = \langle B_i^e, u \rangle_{\Omega^e}. \quad (17)$$

Note that efficiency gains can be had at the expense of accuracy by instead performing the integration in the parametric domain of the element [18].

The element-wise projection produces one control value for each element in the support of the function. These values must be combined in order to provide the final control value. A core component of the Bézier projection algorithm is the definition of an appropriate averaging operation. The process of computing the weights is illustrated in Figure 2. A weighted average of the values is computed using the weighting

$$\omega_a^e = \frac{\int_{\Omega^e} N_a^e d\Omega}{\int_{\Omega^A} N_{A(e,a)} d\Omega} \quad (18)$$

where Ω^e corresponds to the physical domain of element e , $A(e, a)$ is a mapping from a local nodal index a defined over element e to a corresponding global node index A , and Ω^A corresponds to the physical support of N_A . The final averaged global control point is then calculated as

$$P_A = \sum_{\Omega^e \in \Omega^A} \omega_{A(e,a)} P_{A(e,a)}. \quad (19)$$

Bézier projection onto NURBS functions can be defined in an analogous manner [18].

The individual steps comprising the Bézier projection algorithm are illustrated in Figure 3 where the curve defined by $\mathbf{f}(t) = \left(\frac{t}{3}\right)^{3/2} \mathbf{e}_1 + \frac{1}{10} \sin(\pi t) \mathbf{e}_2$, $t \in [0, 3]$ is projected onto the quadratic B-spline basis defined by the knot vector $[0, 0, 0, 1/3, 2/3, 1, 1, 1]$. For this example, the algorithm proceeds as follows:

Step 1: The function \mathbf{f} is projected onto the Bernstein basis of each element. This results in a set of Bézier coefficients that define an approximation to \mathbf{f} . The Bézier coefficients are indicated in part (1) of Figure 3 by square markers that have been colored to match the corresponding element. Each Bézier segment is discontinuous.

Step 2: The element reconstruction operator \mathbf{R}^e is used to convert the Bézier control points into spline control points associated with the basis function segments over each element. The new control points are marked with inverted triangles and again colored to indicate the element with which the control point is associated. The control points occur in clusters. The clusters of control points represent the contributions from multiple elements to a single spline basis function control point.

Step 3: Each cluster of control points is averaged to obtain a single control point by weighting each point in the cluster according to the weighting given in (18). The resulting control points are shown as circles with the relative contribution from each element to each control point indicated by the colored fraction of the control point marker. Colors in Figures 2 and 3 are coordinated to illustrate where the averaging weights come from and their values.

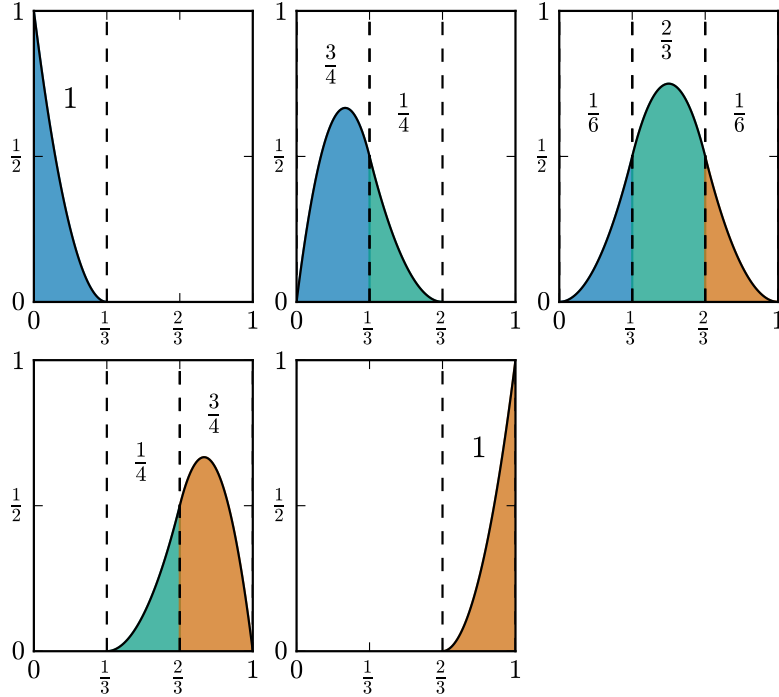


Figure 2: Weights over each knot span associated with the basis function defined by the knot vector $[0, 0, 0, 1/3, 2/3, 1, 1, 1]$.

4.1 Dual basis formulation of Bézier projection

To integrate Bézier projection into a standard finite element assembly algorithm, it is convenient to recast Bézier projection in terms of a dual basis. A dual basis has the distinguishing property that

$$\int_{\Omega} \hat{N}_A N_B d\Omega = \delta_{AB}. \quad (20)$$

Once a dual basis is defined it can be processed in much the same manner as standard basis functions are processed in a finite element code. A complete exposition on the subject of dual bases and the Bézier projection framework can be found in [18]. We first define the dual element extraction operator

$$\hat{\mathbf{D}}^e = \text{diag}(\boldsymbol{\omega}^e) \mathbf{R}^e (\mathbf{G}^e)^{-1} \quad (21)$$

where \mathbf{G}^e is the Gramian matrix of the Bernstein basis functions over the element and $\text{diag}(\boldsymbol{\omega}^e)$ is a diagonal matrix that contains the Bézier projection weights computed by (18). We can then define a dual basis function $\hat{N}_{A(e,a)}$ restricted to element e as

$$\hat{N}_a^e = \sum_j \hat{D}_{aj}^e B_j. \quad (22)$$

The biorthogonality of the dual basis can be seen by noting that

$$\int_{\Omega^e} \hat{\mathbf{N}}^e (\mathbf{N}^e)^T d\Omega = \text{diag}(\boldsymbol{\omega}^e) \quad (23)$$

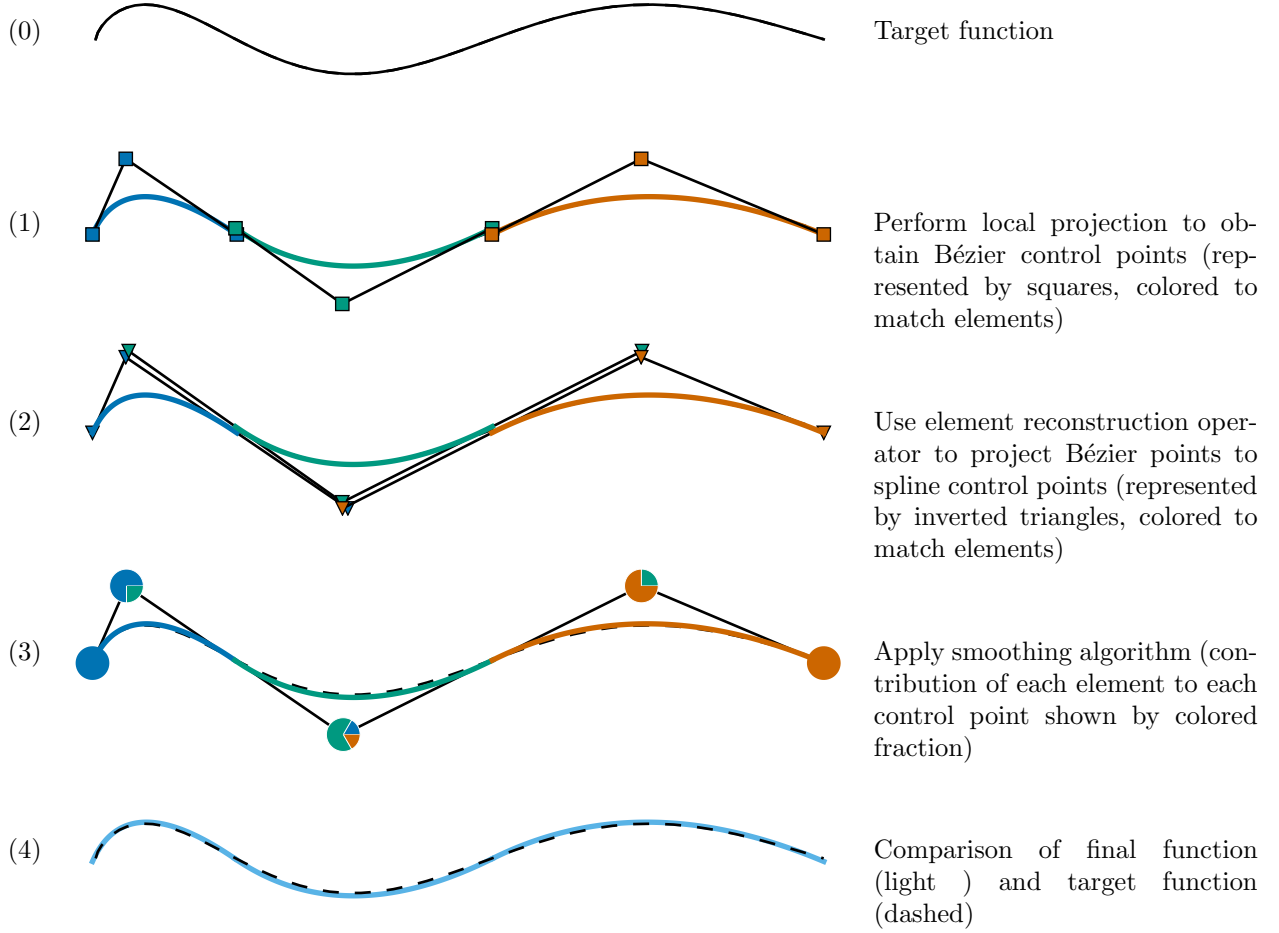


Figure 3: Steps of Bézier projection.

and

$$\mathbf{A}_e \left[\int_{\Omega^e} \hat{\mathbf{N}}^e (\mathbf{N}^e)^T d\Omega \right] = \mathbf{I} \quad (24)$$

where \mathbf{A} is the standard finite element assembly operator [44].

Now, given any function $u \in L^2$ we can use the dual basis to find its representation in terms of the corresponding spline basis as

$$u = \sum_A P_A N_A \quad (25)$$

where

$$P_A = \int_{\Omega^A} \hat{N}_A u d\Omega = \langle \hat{N}_A, u \rangle_{\Omega^A}. \quad (26)$$

A set of dual basis functions corresponding to the quadratic maximally smooth B-spline basis shown in Figure 4a is shown in Figure 4c. Note that these dual functions have compact support and discontinuities which coincide with the underlying knots in the knot vector. The compact support of the dual basis functions will be crucial for maintaining the sparsity of the stiffness matrix for the Bézier \bar{B} formulations presented in this paper. For comparison, the dual basis corresponding to *global* L^2 projection are shown in Figure 4b. Each of these dual basis functions has global support which explains why the use of global \bar{B} projections results in dense stiffness matrices.

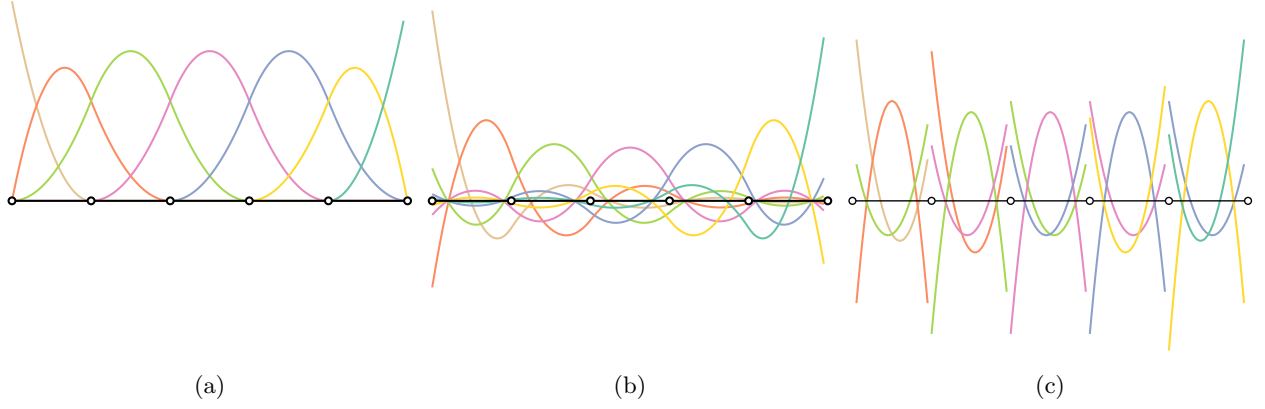


Figure 4: A set of quadratic B-spline basis functions (a), and corresponding dual basis functions computed by a global L^2 projection (b) and the dual basis functions computed using Bézier projection (c). Note that the support of the dual basis functions in (b) is not compact. The dual basis functions shown in (c) have compact support but are not continuous.

4.1.1 Rational dual basis functions

If rational basis functions are used, the construction of the dual basis must be modified slightly. A rational dual basis must satisfy the biorthogonality requirement

$$\int_{\Omega} \bar{R}_A R_B d\Omega = \delta_{AB}. \quad (27)$$

A simple way to achieve biorthogonality is to define

$$\bar{R}_A = W \bar{N}_A \quad (28)$$

where W is the rational weight given in (5). Now

$$\int_{\Omega} \bar{R}_A R_B d\Omega = \int_{\Omega} \bar{N}_A N_B d\Omega = \delta_{AB}. \quad (29)$$

5 Geometric locking: Timoshenko beams

To illustrate the use of Bézier \bar{B} projection to overcome geometric locking effects we study transverse shear locking in Timoshenko beams. The Timoshenko beam problem provides a simple one dimensional setting in which to describe Bézier \bar{B} projection. Note however, that the approach can be directly generalized to more complex settings like spatial beams and shells and other geometric locking mechanisms like membrane locking. We consider a planar cantilevered Timoshenko beam as shown in Figure 5. The strong form for this problem can be stated as

$$\left. \begin{aligned} -sGA\gamma' &= f(x) \\ -EI\kappa' - sGA\gamma &= 0 \\ \kappa &= \phi' \\ \gamma &= \omega' - \phi \end{aligned} \right\} \text{in } \Omega \quad (30)$$

$$\left. \begin{aligned} \omega &= 0 \\ \phi &= 0 \end{aligned} \right\} \text{at } x = 0 \quad (31)$$

$$\left. \begin{aligned} sAG\gamma &= Q \\ -EI\kappa &= M \end{aligned} \right\} \text{at } x = L \quad (32)$$

where γ is the shear strain, κ is the bending strain, ω is the vertical displacement, ϕ is the angle of rotation of the normal to the mid-plane of the beam, f is the distributed transverse load, Q is a point load, M is the moment, E is the Young's modulus, G is the shear modulus, A is the cross-sectional area, I is the second moment of inertia of the beam cross-section, s is the shear correction factor, normally set to $5/6$ for rectangular cross-sections, and $\Omega = (0, L)$. When ω and ϕ are interpolated by basis functions of the same order the finite element solution to this problem exhibits shear locking as the beam becomes slender.

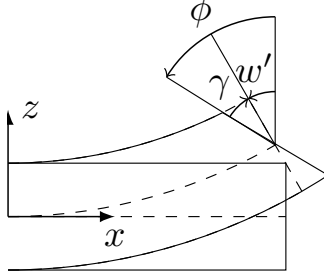


Figure 5: Deformation of a Timoshenko beam. The normal rotates by the angle ϕ , which is not equal to w' , due to shear deformation.

5.1 Symmetric Bézier \bar{B} projection

Locking is caused in Timoshenko beam problems when equal order interpolation is used for both midline displacements and rotations. To reduce the effects of locking for these problems the \bar{B} method projects the shear strain, γ , onto a lower order function space. This process produces a projected shear strain, which we call $\bar{\gamma}$, that is substituted into the weak form of the problem statement. In this section we use the Bézier projection operator to compute an approximation of $\bar{\gamma}$, and refer to this approach as the symmetric Bézier \bar{B} projection method because the resulting stiffness matrix is symmetric.

5.1.1 The weak form

Given the function spaces $\mathcal{S}(\Omega) = \{\mathbf{u} \mid \mathbf{u} \in H^1(\Omega) \times H^1(\Omega), \mathbf{u}|_{\Gamma_g} = \mathbf{g}\}$ and $\mathcal{V}(\Omega) = \{\mathbf{w} \mid \mathbf{w} \in H^1(\Omega) \times H^1(\Omega), \mathbf{w}|_{\Gamma_g} = \mathbf{0}\}$ where $\mathbf{u} = \{\omega, \phi\}^T$, $\mathbf{w} = \{\delta\omega, \delta\phi\}^T$, \mathbf{g} is the prescribed Dirichlet boundary condition, and Γ_g is the Dirichlet boundary at $x = 0$, the weak form of the problem can be stated as: find $\mathbf{u} \in \mathcal{S}(\Omega)$ such that for all $\mathbf{w} \in \mathcal{V}(\Omega)$

$$\int_0^L \kappa(\mathbf{w})EI\kappa(\mathbf{u}) + \bar{\gamma}(\mathbf{w})sGA\bar{\gamma}(\mathbf{u}) dx = \int_0^L \delta\omega f dx + \delta\omega(L)Q + \delta\phi(L)M. \quad (33)$$

5.1.2 Discretization

We discretize ω and ϕ as

$$\omega = \sum_A \omega_A N_A \quad (34)$$

$$\phi = \sum_A \phi_A N_A \quad (35)$$

where N_A is a degree p spline basis function and ω_A and ϕ_A are the corresponding control point values. The shear strain and bending strain can then be expressed as

$$\gamma = \sum_A [N'_A \quad -N_A] [\omega_A \quad \phi_A]^T \quad (36)$$

$$\kappa = \sum_A [0 \quad N'_A] [\omega_A \quad \phi_A]^T \quad (37)$$

The shear strain $\bar{\gamma}$ is constructed by Bézier projection of the true shear strain γ onto a lower degree space. In other words, we project from a p^{th} degree spline space with n basis functions \mathbf{N} defined by the knot vector

$$\bar{\mathbf{\Xi}}_p = \{\underbrace{0, 0, \dots, 0}_{p+1 \text{ copies}}, \bar{\mathbf{\Xi}}_{int}, \underbrace{1, 1, \dots, 1}_{p+1 \text{ copies}}\}, \quad (38)$$

onto a $p-1^{th}$ degree spline space with \bar{n} basis functions $\bar{\mathbf{N}}$ defined by the knot vector

$$\bar{\bar{\mathbf{\Xi}}}_{p-1} = \{\underbrace{0, 0, \dots, 0}_p, \bar{\mathbf{\Xi}}_{int}, \underbrace{1, 1, \dots, 1}_p\} \quad (39)$$

where the internal knots, denoted by $\bar{\mathbf{\Xi}}_{int}$, are the same for both spaces. The projected shear strain $\bar{\gamma}$ can then be written as

$$\bar{\gamma} = \sum_A \bar{\gamma}_A \bar{N}_A. \quad (40)$$

The control variables $\bar{\gamma}_A$ are simply

$$\bar{\gamma}_A = \int_{\Omega^A} \hat{N}_A \gamma \, d\Omega = \langle \hat{N}_A, \gamma \rangle_{\Omega^A} \quad (41)$$

where \hat{N}_A is a dual basis function for the spline space of degree $p-1$ computed from (22).

Localizing to the Bézier element we define the strain-displacement arrays in terms of element Bernstein basis functions of degree p and $p-1$ as

$$\mathbf{B}_e^\kappa = [0 \quad -B_{0,p}^{e'} \quad \cdots \quad 0 \quad -B_{p,p}^{e'}], \quad (42)$$

$$\mathbf{B}_e^\gamma = [B_{0,p}^{e'} \quad -B_{0,p}^{e'} \quad \cdots \quad B_{p,p}^{e'} \quad -B_{p,p}^{e'}], \quad (43)$$

$$\bar{\mathbf{B}}_e = [\bar{B}_{0,p-1}^e \quad \cdots \quad \bar{B}_{p-1,p-1}^e], \quad (44)$$

where $B_{i,p}^e$ is the i^{th} Bernstein basis function of order p . We can then compute the element arrays as

$$\mathbf{K}_e^b = EIC^e \langle \mathbf{B}_e^{\kappa T}, \mathbf{B}_e^\kappa \rangle (\mathbf{C}^e)^T, \quad (45)$$

$$\bar{\mathbf{M}}_e = sGA\bar{\mathbf{C}}^e \langle \bar{\mathbf{B}}_e^T, \bar{\mathbf{B}}_e \rangle (\bar{\mathbf{C}}^e)^T, \quad (46)$$

$$\hat{\mathbf{P}}_e = \langle (\hat{\mathbf{N}}^e)^T, \mathbf{B}_e^\gamma \rangle (\mathbf{C}^e)^T, \quad (47)$$

where \mathbf{C}^e is the element extraction operator for the degree p spline space, $\bar{\mathbf{C}}^e$ is the element extraction operator for the degree $p-1$ spline space, and $\hat{\mathbf{N}}^e$ are the dual basis functions restricted to the element for the degree $p-1$ spline space. The global stiffness matrix can then be written as

$$\mathbf{K} = \mathbf{K}^b + \bar{\mathbf{K}}^s \quad (48)$$

where

$$\mathbf{K}^b = \mathbf{A}_e \mathbf{K}_e^b, \quad (49)$$

$$\bar{\mathbf{K}}^s = \hat{\mathbf{P}}^T \bar{\mathbf{M}} \hat{\mathbf{P}} \quad (50)$$

$$\hat{\mathbf{P}} = \mathbf{A}_e \hat{\mathbf{P}}_e \quad (51)$$

$$\bar{\mathbf{M}} = \mathbf{A}_e \bar{\mathbf{M}}_e \quad (52)$$

and \mathbf{A} is the standard finite element assembly operator [44]. We note that the assembly of $\bar{\mathbf{K}}^s$ requires the assembly of two intermediate matrices, $\bar{\mathbf{M}}$ and $\hat{\mathbf{P}}$. The computation of these matrices is needed because the product of two integrals over the entire domain can not be localized to the element level.

5.2 Non-symmetric Bézier \bar{B} projection

Simo and Hughes [28] have shown that \bar{B} formulations and mixed formulations are equivalent. However, the development of the symmetric Bézier \bar{B} projection method presented in Section 5.1, where we began by interpreting the \bar{B} formulation as a strain projection method, lacks a connection to mixed formulations. In this section, we present a second method based on Bézier projection in which we view the \bar{B} formulation as a mixed formulation where, for the Timoshenko beam problem, the auxiliary variable is the shear strain. We use the Bézier dual basis functions as the test functions for the auxiliary variable. Once the problem has been cast as a mixed formulation we then eliminate the auxiliary variable to get a purely displacement based formulation. This approach preserves convergence rates and all assembly routines for the stiffness matrix can be performed at the element level. However, it does not produce a symmetric stiffness matrix.

5.2.1 The weak form

In the mixed formulation for the Timoshenko beam problem the shear stress, $\tau = sGA\gamma$, is taken as a new independent variable. The weak form of the mixed formulation can then be stated as: find $\mathbf{u} \in \mathcal{S}(\Omega)$ and $\tau \in L^2(\Omega)$ such that for all $\mathbf{w} \in \mathcal{V}(\Omega)$ and $\delta\tau \in L^2(\Omega)$

$$\int_0^L \kappa(\mathbf{w}) EI \kappa(\mathbf{u}) + \gamma(\mathbf{w}) \tau \, dx = l \langle \mathbf{w} \rangle \quad (53)$$

$$\int_0^L \delta\tau (sGA\gamma(\mathbf{u}) - \tau) \, dx = 0. \quad (54)$$

5.2.2 Discretization

In the finite element formulation of the mixed problem, the discretization of \mathbf{u} and \mathbf{w} remain the same as before. The shear strain and its variation, however, are in $L^2(\Omega)$, so their finite element approximation can consist of functions with lower regularity, such as discontinuous polynomials. When the field \mathbf{u} is discretized by p^{th} degree spline basis functions defined by the knot vector given in (38), we use the $p - 1$ degree spline basis functions, defined by the knot vector given in (39), to discretize the shear stress τ and the corresponding dual basis to discretize its variation $\delta\tau$. The discrete form of the shear stress and its variation are given by

$$\tau = \sum_A \tau_A \bar{N}_A \quad (55)$$

$$\delta\tau = \sum_A \delta\tau_A \hat{N}_A. \quad (56)$$

The stiffness matrix for the mixed form can then be written as

$$\mathbf{K}_{mix} = \begin{bmatrix} \mathbf{K}^b & \mathbf{P}^T \\ sG\mathbf{A}\hat{\mathbf{P}} & -\mathbf{I} \end{bmatrix} \quad (57)$$

where

$$\mathbf{P} = \mathbf{A} \mathbf{P}_e, \quad (58)$$

and

$$\mathbf{P}_e = \bar{\mathbf{C}}^e \langle \bar{\mathbf{B}}_e^T, \mathbf{B}_e \rangle (\mathbf{C}^e)^T. \quad (59)$$

and $\hat{\mathbf{P}}$ is given in (47) and (51). We can now eliminate the control variable of the shear stress from (57) to get a pure displacement formulation where the stiffness matrix can be written as

$$\mathbf{K} = \mathbf{K}^b + \bar{\mathbf{K}}_{NS}^s, \quad (60)$$

where

$$\bar{\mathbf{K}}_{NS}^s = sG\mathbf{A}\mathbf{P}^T\hat{\mathbf{P}}. \quad (61)$$

We can see that the use of different function spaces for the shear strain and its variation leads to a non-symmetric stiffness matrix.

Remark As mentioned previously, the symmetric Bézier \bar{B} formulation is not consistent with a mixed formulation. To see this, we can recover the mixed formulation of (48), which is

$$\begin{bmatrix} \mathbf{K}^b & \hat{\mathbf{P}}^T \\ sG\mathbf{A}\hat{\mathbf{P}} & -\bar{\mathbf{M}}^{-1} \end{bmatrix}, \quad (62)$$

where both the shear stress and its variation are discretized by the dual basis functions. However, for the inner product of dual basis functions we have

$$\langle \hat{N}_i, \hat{N}_j \rangle \neq \bar{\mathbf{M}}_{ij}^{-1}, \quad (63)$$

which shows the inconsistency between the symmetric Bézier \bar{B} formulation and the mixed formulation.

5.3 Bandwidth of the stiffness matrix

A global \bar{B} method that utilizes a global L^2 projection results in a dense stiffness matrix. The Bézier \bar{B} methods, on the other hand, produce sparse stiffness matrices. However, the coupling of the local dual basis functions does increase the bandwidth slightly. This is illustrated in Figure 6, which shows the structure of the stiffness matrix for the Timoshenko beam problem using the second order basis functions of maximal smoothness for a displacement-based method (Figure 6a), global \bar{B} method (Figure 6b), symmetric Bézier \bar{B} method (Figure 6c) and non-symmetric Bézier \bar{B} method (Figure 6d). The blank cells indicate zero terms in the matrix while colored cells show the location of nonzero terms. The increased bandwidth of the symmetric Bézier \bar{B} method when compared to a displacement-based method can be explained by looking at the product of the integrals in (50). For example, if we consider the basis functions N_1 and N_5 in Figure 7 we see that $\text{supp}(N_1) \cap \text{supp}(N_5) = \emptyset$, which means that the inner product of these two functions will be zero and the corresponding coefficient in the stiffness matrix will be zero in the displacement-based method. For the Bézier \bar{B} method, however, the form of (50) leads to a coupling between N_1 and N_5 . This can be seen by considering Ω_2 . Over this element, the shear stiffness can be represented as

$$\bar{\mathbf{K}}_2^s = \sum_{i=1}^3 \sum_{j=1}^3 \mathbf{P}_i^T \bar{\mathbf{M}}_2 \mathbf{P}_j \quad (64)$$

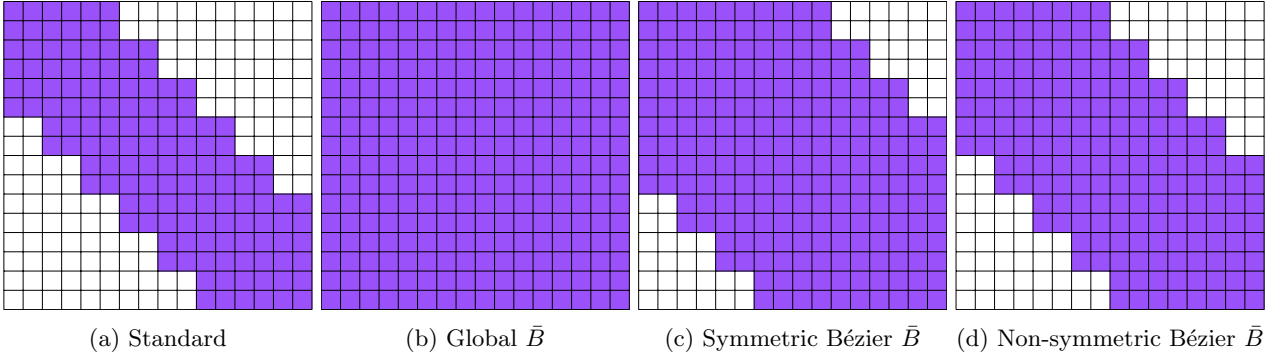


Figure 6: Illustrations of the structure of 2^{nd} order Timoshenko beam stiffness matrices for (a) a standard displacement method, (b) a global \bar{B} method, (c) a symmetric Bézier \bar{B} method and (d) a non-symmetric Bézier \bar{B} method.

and the term of this summation that results in the coupling between N_1 and N_5 is $\mathbf{P}_1^T \bar{\mathbf{M}}_2 \mathbf{P}_3$, where \mathbf{P}_1 is the inner product of N_1 and \hat{N}_2 , \mathbf{P}_3 is the inner product of N_5 and \hat{N}_3 , and $\bar{\mathbf{M}}_2$ is the inner product of \bar{N}_2 and \bar{N}_3 . We can see from Figure 7 that $\text{supp}(N_1) \cap \text{supp}(\hat{N}_2) = \Omega_1$, $\text{supp}(N_5) \cap \text{supp}(\hat{N}_3) = \Omega_3$ and $\text{supp}(\bar{N}_2) \cap \text{supp}(\bar{N}_3) = \Omega_2$, so that $\mathbf{P}_1^T \bar{\mathbf{M}}_2 \mathbf{P}_3$ is not zero. Thus we have increased the number of nonzero coefficients in the shear stiffness matrix. However, the same exercise can be used to show that there is no coupling between N_0 and N_6 for this set of basis functions so the matrix is not dense. the bandwidth of the non-symmetric Bézier \bar{B} method is reduced further. This is because the Gramian matrix does not appear in the this formulation. In fact, from the formulation of the element stiffness matrix, we can show that the bandwidth of the stiffness matrix of the symmetric Bézier \bar{B} and non-symmetric Bézier \bar{B} methods for the Timoshenko beam are $6p - 3$ and $4p - 1$, respectively.

Remark In [41] a local \bar{B} method for shells was proposed that was based on the local least squares method presented in [43]. This approach has a similar structure to the symmetric Bézier \bar{B} method presented here. However, it was shown in [18] that choosing (18) as the weighting provides a significant increase in the accuracy of the approximation.

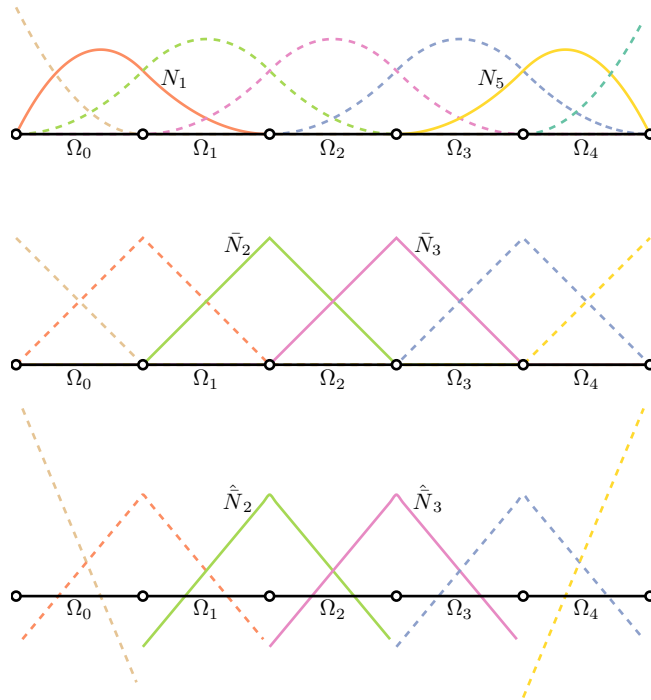


Figure 7: Quadratic maximally smooth B-spline basis functions (top), associated linear basis functions (middle), and dual basis functions (bottom) for the Bézier \bar{B} formulation.

5.4 Numerical results

In our study, a straight planar cantilever beam is clamped on the left end and a sinusoidal distributed load $f(x) = \sin(\pi \frac{x}{l})$ is applied, as depicted in Figure 8. The analytical solution for vertical displacement w , rotation ϕ , bending moment M , and transverse shear force Q are given by

$$\begin{aligned} w(x) &= \frac{EI (6\pi^2 l^2 \sin(\frac{\pi x}{l}) + 6\pi^3 l x) + sGA (6l^4 \sin(\frac{\pi x}{l}) - 6\pi l^3 x + 3\pi^3 l^2 x^2 - \pi^3 l x^3)}{6\pi^4 sEIGA} \\ \phi(x) &= \frac{2l^3 \cos(\frac{\pi x}{l}) - 2l^3 + 2\pi^2 l^2 x - \pi^2 l x^2}{2\pi^3 EI} \\ M(x) &= \frac{l^2 \sin(\frac{\pi x}{l}) - \pi l^2 + \pi l x}{\pi^2} \\ Q(x) &= \frac{-l \cos(\frac{\pi x}{l}) - l}{\pi}. \end{aligned} \tag{65}$$

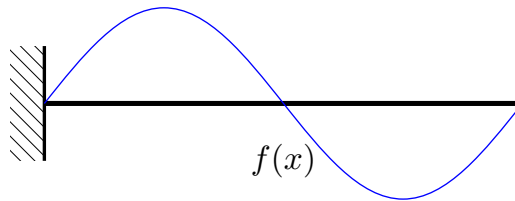


Figure 8: Straight planar cantilevered Timoshenko beam clamped at the left and loaded by a distributed load $f(x)$.

The beam has a rectangular cross-section and we use the following non-dimensional sectional and material parameters: length $l = 10$, width $b = 1$, thickness $t = 0.01$, Young's modulus $E = 10^9$, Poisson's ratio $\nu = 0.3$, and a shear correction factor of $s = 5/6$. A comparison of the normalized error in the L^2 norm for w , ϕ , M and Q versus the number of degrees of freedom for polynomial degrees $p = 1, 2, 3$ is shown in Figure 9. Results computed using standard finite elements are labeled Q_1 , Q_2 , and Q_3 . Results computed using a global \bar{B} method are labeled \mathcal{T}^{L^2} , those computed with the symmetric Bézier \bar{B} method and the non-symmetric Bézier \bar{B} method are labeled $S - \mathcal{T}^P$ and $NS - \mathcal{T}^P$, respectively. As expected, the Q_1 results lock and the error remains virtually unchanged as the mesh is refined. Increasing the polynomial degree does reduce the locking effect, although the reduction is minor for the Q_2 results. \mathcal{T}^{L^2} , $S - \mathcal{T}^P$ and $NS - \mathcal{T}^P$ are essentially locking free for all polynomial orders. The convergence rates for the \bar{B} methods are at least $p + 1$ for w , p for ϕ , $p - 1$ for M , and $p - 2$ for Q . These rates agree with those reported in [45] and are optimal. To reiterate, Bézier \bar{B} methods produces the same convergence rates as the global \bar{B} method and the the error plots of $NS - \mathcal{T}^P$ for ϕ , M and Q are identical to those of \mathcal{T}^{L^2} .

We have also studied the relationship between shear locking and decreasing slenderness ratios for $p = 2$. The results are shown in Figure 10. For all three methods, the number of degrees of freedom are fixed, and the sectional and material parameters are the same as in the previous study. The slenderness ratio varies from 10 to 5×10^3 . Q_2 locks severely. The \bar{B} methods, on the other hand, are locking free.

6 Volumetric locking: Nearly incompressible linear elasticity

To demonstrate the use of Bézier \bar{B} methods to alleviate volumetric locking effects we study the nearly incompressible elasticity problem in two dimensions. We start with the small strain tensor ε , which is defined as the symmetric part of the displacement gradient, i.e.,

$$\varepsilon_{ij} = \frac{u_{i,j} + u_{j,i}}{2}. \tag{66}$$

The stress tensor is related to the strain tensor through the generalized Hooke's law

$$\sigma_{ij} = c_{ijkl} \varepsilon_{kl} \tag{67}$$

where, for isotropic elasticity, the elastic coefficients and stress tensor can be expressed in terms of the Lamé parameters λ and μ as

$$c_{ijkl} = \mu(\delta_{ik}\delta_{jl} + \delta_{il}\delta_{jk}) + \lambda\delta_{ij}\delta_{kl} \tag{68}$$

$$\sigma_{ij} = \lambda\varepsilon_{kk}\delta_{ij} + 2\mu\varepsilon_{ij}. \tag{69}$$

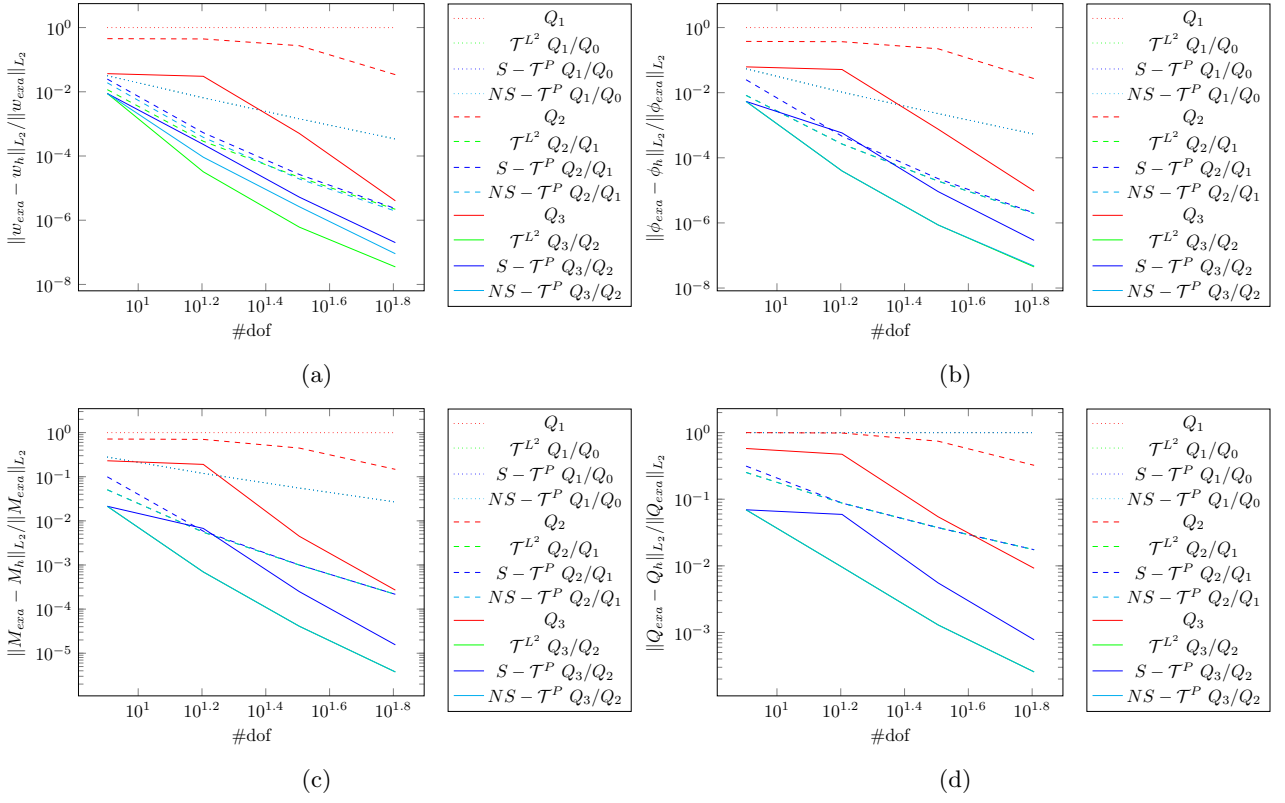


Figure 9: Convergence studies for slenderness factor $l/t = 10^{-3}$. Error in the L^2 -norm for (a) displacement w , (b) rotation ϕ , (c) bending moment M , and (d) shear force Q .

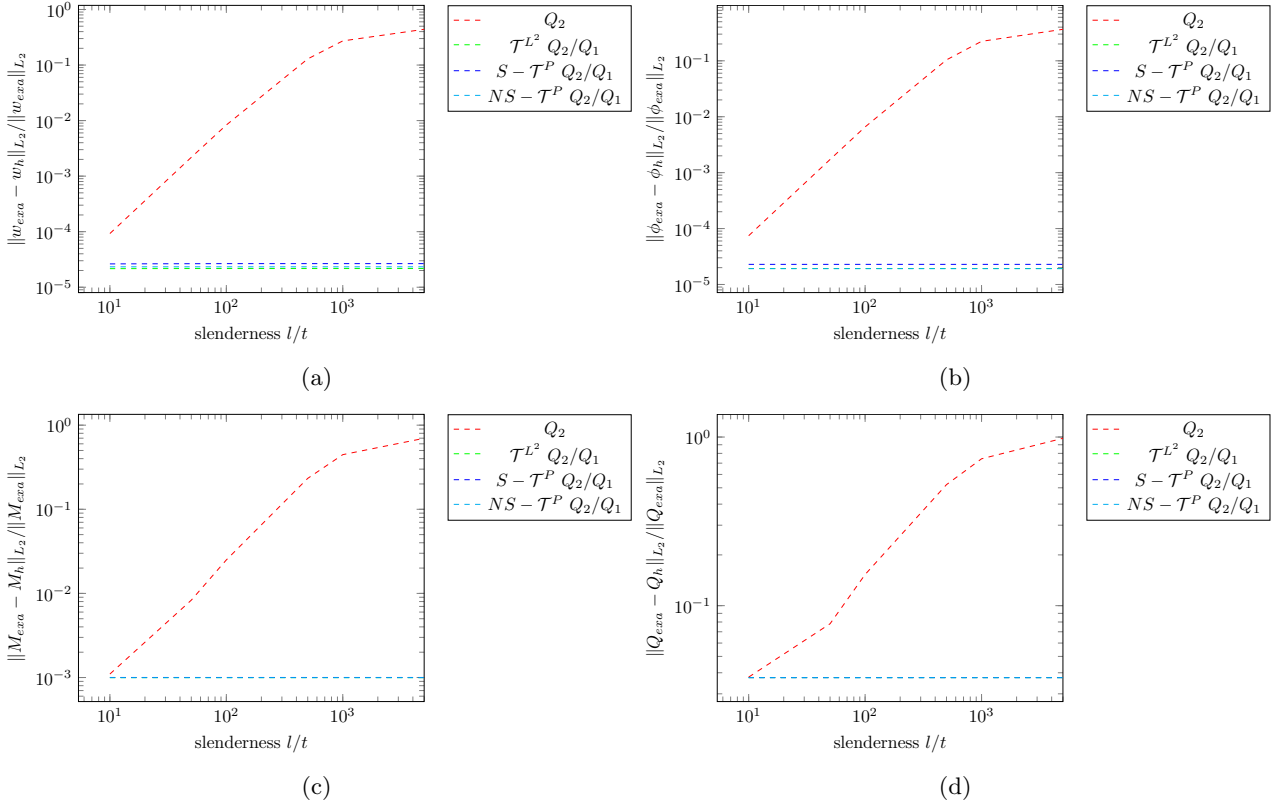


Figure 10: Convergence study for increasing slenderness, $p = 2$, and $\#dof = 32$. Error in the L^2 -norm for (a) displacement w , (b) rotation ϕ , (c) bending moment M , and (d) shear force Q .

The Lamé parameters λ and μ are defined in terms of Young's modulus, E , and Poisson's ratio, ν , as

$$\lambda = \frac{\nu E}{(1 + \nu)(1 - 2\nu)} \quad (70)$$

$$\mu = \frac{\nu E}{2(1 + \nu)}. \quad (71)$$

we can write the strong form of linear elasticity as

$$\sigma_{ij,j} + f_i = 0 \text{ in } \Omega \quad (72)$$

$$u_i = g_i \text{ on } \Gamma_{g_i} \quad (73)$$

$$\sigma_{ij}n_j = h_i \text{ on } \Gamma_{h_i} \quad (74)$$

where Dirichlet boundary conditions are applied on Γ_{g_i} , Neumann boundary conditions are applied on Γ_{h_i} , and the closure of the domain Ω is $\bar{\Omega} = \Omega \cup \Gamma_{g_i} \cup \Gamma_{h_i}$. To demonstrate the source of volumetric locking, we introduce the pressure term

$$p = -(\lambda + 2\mu/3)\epsilon_{ii}. \quad (75)$$

If $\nu \rightarrow \frac{1}{2}$ then λ becomes very large and the additional constraint $\epsilon_{ii} = 0$ is applied to the volumetric strain.

6.1 Symmetric Bézier \bar{B} projection

6.1.1 The weak form

The \bar{B} approach for nearly incompressible linear elasticity splits the strain tensor ϵ into volumetric and deviatoric strains and then replaces the volumetric strain with a projected strain. We begin with

$$\epsilon(\mathbf{u}) = \epsilon^{vol}(\mathbf{u}) + \epsilon^{dev}(\mathbf{u}) \quad (76)$$

where $\epsilon^{vol} = \frac{1}{3}\text{tr}(\epsilon)\mathbf{I}$ is the volumetric strain and $\epsilon^{dev} = \epsilon - \frac{1}{3}\text{tr}(\epsilon)\mathbf{I}$ is the deviatoric strain. The volumetric strain is then replaced by a projected volumetric strain $\bar{\epsilon}^{vol}$ and the new total strain becomes

$$\bar{\epsilon} = \bar{\epsilon}^{vol} + \epsilon^{dev}. \quad (77)$$

The weak form can then be written as: find $\mathbf{u} \in \mathcal{S}(\Omega)$ such that for all $\mathbf{w} \in \mathcal{V}(\Omega)$

$$\bar{a}(\mathbf{w}, \mathbf{u}) = \bar{l}(\mathbf{w}) \quad (78)$$

where

$$\bar{a}(\mathbf{w}, \mathbf{u}) = \int_{\Omega} \bar{\epsilon}_{ij}(\mathbf{w})c_{ijkl}\bar{\epsilon}_{kl}(\mathbf{u})d\Omega, \quad (79)$$

$$\bar{l}(\mathbf{w}) = \int_{\Omega} \mathbf{w} \cdot \mathbf{f}d\Omega + \int_{\Gamma_h} \mathbf{w} \cdot \mathbf{h}d\Gamma. \quad (80)$$

6.1.2 Discretization

Following the same approach as was described for Timoshenko beams in Section 5 we define element level strain-displacement matrices in terms of the Bernstein basis

$$\mathbf{B}_e^{dev} = \begin{bmatrix} \frac{2}{3} \frac{\partial B_{0,p}^e}{\partial x} & -\frac{1}{3} \frac{\partial B_{0,p}^e}{\partial y} & -\frac{1}{3} \frac{\partial B_{0,p}^e}{\partial z} & \dots & \frac{2}{3} \frac{\partial B_{p,p}^e}{\partial x} & -\frac{1}{3} \frac{\partial B_{p,p}^e}{\partial y} & -\frac{1}{3} \frac{\partial B_{p,p}^e}{\partial z} \\ \frac{1}{3} \frac{\partial B_{0,p}^e}{\partial x} & \frac{2}{3} \frac{\partial B_{0,p}^e}{\partial y} & \frac{1}{3} \frac{\partial B_{0,p}^e}{\partial z} & \dots & \frac{1}{3} \frac{\partial B_{p,p}^e}{\partial x} & \frac{2}{3} \frac{\partial B_{p,p}^e}{\partial y} & \frac{1}{3} \frac{\partial B_{p,p}^e}{\partial z} \\ \frac{3}{3} \frac{\partial x}{\partial x} & \frac{3}{3} \frac{\partial y}{\partial y} & -\frac{3}{3} \frac{\partial z}{\partial z} & \dots & -\frac{3}{3} \frac{\partial x}{\partial x} & \frac{3}{3} \frac{\partial y}{\partial y} & -\frac{3}{3} \frac{\partial z}{\partial z} \\ \frac{1}{3} \frac{\partial B_{0,p}^e}{\partial x} & -\frac{1}{3} \frac{\partial B_{0,p}^e}{\partial y} & \frac{2}{3} \frac{\partial B_{0,p}^e}{\partial z} & \dots & -\frac{1}{3} \frac{\partial B_{p,p}^e}{\partial x} & \frac{1}{3} \frac{\partial B_{p,p}^e}{\partial y} & \frac{2}{3} \frac{\partial B_{p,p}^e}{\partial z} \\ \frac{3}{3} \frac{\partial x}{\partial x} & \frac{3}{3} \frac{\partial y}{\partial y} & \frac{3}{3} \frac{\partial z}{\partial z} & \dots & \frac{3}{3} \frac{\partial x}{\partial x} & \frac{3}{3} \frac{\partial y}{\partial y} & \frac{3}{3} \frac{\partial z}{\partial z} \\ 0 & \frac{\partial B_{0,p}^e}{\partial z} & \frac{\partial B_{0,p}^e}{\partial z} & \dots & 0 & \frac{\partial B_{p,p}^e}{\partial z} & \frac{\partial B_{p,p}^e}{\partial z} \\ \frac{\partial B_{0,p}^e}{\partial x} & 0 & \frac{\partial B_{0,p}^e}{\partial y} & \dots & \frac{\partial B_{p,p}^e}{\partial x} & 0 & \frac{\partial B_{p,p}^e}{\partial y} \\ \frac{\partial z}{\partial B_{0,p}^e} & \frac{\partial B_{0,p}^e}{\partial x} & \frac{\partial y}{\partial B_{0,p}^e} & \dots & \frac{\partial z}{\partial B_{p,p}^e} & \frac{\partial B_{p,p}^e}{\partial x} & \frac{\partial x}{\partial B_{p,p}^e} \\ \frac{\partial y}{\partial B_{0,p}^e} & \frac{\partial x}{\partial B_{0,p}^e} & 0 & \dots & \frac{\partial y}{\partial B_{p,p}^e} & \frac{\partial x}{\partial B_{p,p}^e} & 0 \end{bmatrix}, \quad (81)$$

$$\mathbf{B}_e^{vol} = \begin{bmatrix} \frac{\partial B_{0,p}^e}{\partial x} & \frac{\partial B_{0,p}^e}{\partial y} & \frac{\partial B_{0,p}^e}{\partial z} & \dots & \frac{\partial B_{p,p}^e}{\partial x} & \frac{\partial B_{p,p}^e}{\partial y} & \frac{\partial B_{p,p}^e}{\partial z} \end{bmatrix} \quad (82)$$

The deviatoric part of the element stiffness matrix can then be computed from the corresponding strain-displacement matrices as

$$\mathbf{K}_e^{dev} = \mathbf{C}^e \langle \mathbf{B}_e^{devT} \mathbf{D} \mathbf{B}_e^{dev} \rangle (\mathbf{C}^e)^T. \quad (83)$$

where \mathbf{C}^e is the element extraction operator for the degree p spline space. The volumetric part of the stiffness matrix is computed using Bezier projection. The intermediate element matrices are

$$\bar{\mathbf{M}}_e^{vol} = \bar{\mathbf{C}}^e \langle \bar{\mathbf{B}}_e^T, \frac{1}{3}(3\lambda + 2\mu)\bar{\mathbf{B}}_e \rangle (\bar{\mathbf{C}}^e)^T \quad (84)$$

$$\hat{\mathbf{P}}_e^{vol} = \langle (\hat{\mathbf{N}}^e)^T, \mathbf{B}_e^{vol} \rangle (\mathbf{C}^e)^T \quad (85)$$

where $\bar{\mathbf{C}}^e$ is the element extraction operator for the degree $p-1$ spline space, $\hat{\mathbf{N}}^e$ are the dual basis functions restricted to the element, and

$$\bar{\mathbf{B}}_e = [B_{0,p-1}^e \quad \dots \quad B_{p-1,p-1}^e]. \quad (86)$$

The global stiffness matrix can then be assembled as

$$\mathbf{K} = \mathbf{K}^{dev} + \bar{\mathbf{K}}_S^{vol} \quad (87)$$

where

$$\mathbf{K}^{dev} = \mathbf{A}_e \mathbf{K}_e^{dev}, \quad (88)$$

$$\bar{\mathbf{K}}_S^{vol} = \hat{\mathbf{P}}^T \bar{\mathbf{M}} \hat{\mathbf{P}} \quad (89)$$

$$\hat{\mathbf{P}} = \mathbf{A}_e \hat{\mathbf{P}}_e^{vol} \quad (90)$$

$$\bar{\mathbf{M}} = \mathbf{A}_e \bar{\mathbf{M}}_e^{vol}. \quad (91)$$

6.2 Non-symmetric Bézier \bar{B} projection

6.2.1 The weak form

A mixed formulation for nearly incompressible elasticity can be developed by considering the pressure p as an independent variable. The weak statement of the problem is then given as: find $\mathbf{u} \in \mathcal{S}(\Omega)$ and $p \in L^2(\Omega)$ such that for all $\mathbf{w} \in \mathcal{V}(\Omega)$ and $\delta p \in L^2(\Omega)$

$$\hat{a}\langle \mathbf{w}, \mathbf{u} \rangle - b\langle \mathbf{w}, p \rangle = l\langle \mathbf{w} \rangle, \quad (92)$$

$$-b\langle \mathbf{u}, \delta p \rangle - \frac{1}{(\lambda + 2\mu/3)} \int_{\Omega} \delta p p d\Omega = 0, \quad (93)$$

where

$$\hat{a}\langle \mathbf{w}, \mathbf{u} \rangle = \int_{\Omega} \epsilon_{ij}(\mathbf{w}) \hat{c}_{ijkl} \epsilon_{kl}(\mathbf{u}) d\Omega, \quad (94)$$

$$\hat{c}_{ijkl} = \mu(\delta_{ik}\delta_{jl} + \delta_{il}\delta_{jk} - 2/3\delta_{ij}\delta_{kl}), \quad (95)$$

$$b\langle \mathbf{w}, p \rangle = \int_{\Omega} \epsilon_{ii}(\mathbf{w}) p d\Omega. \quad (96)$$

6.2.2 Discretization

Following the same pattern as the non-symmetric Bézier \bar{B} method for the Timoshenko beam problem, we use the same discretization for \mathbf{u} and \mathbf{w} and use lower order spline basis functions and corresponding dual basis functions for the discretization of the pressure p and its variation δp , respectively. The discretized stiffness matrix in mixed form can be written as

$$\mathbf{K}_{mix} = \begin{bmatrix} \mathbf{K}^{dev} & -\mathbf{P}^T \\ -\hat{\mathbf{P}} & -\frac{1}{(\lambda + 2\mu/3)} \mathbf{I} \end{bmatrix}, \quad (97)$$

where

$$\mathbf{P} = \mathbf{A}_e \mathbf{P}_e^{vol}, \quad (98)$$

Table 1: Weights for the plate with a circular hole

i	$w_{i,1}$	$w_{i,2}$	$w_{i,3}$
1	1	$1/\sqrt{2}$	1
2	1	$1/\sqrt{2}$	1
3	1	$1/\sqrt{2}$	1

Table 2: Control points for the plate with a circular hole

i	$B_{i,1}$	$B_{i,2}$	$B_{i,3}$
1	(0,1)	(1,1)	(1,0)
2	(0,2.5)	(2.5,2.5)	(2.5,0)
3	(0,4)	(4,4)	(4,0)

with

$$\mathbf{P}_e^{vol} = \bar{\mathbf{C}}^e \langle \bar{\mathbf{B}}_e^T, \mathbf{B}_e^{vol} \rangle (\mathbf{C}^e)^T. \quad (99)$$

By eliminating the pressure control variables, we obtain a pure displacement formulation with the stiffness matrix taking the form

$$\mathbf{K} = \mathbf{K}^{dev} + \bar{\mathbf{K}}_{NS}^{vol}, \quad (100)$$

where

$$\bar{\mathbf{K}}_{NS}^{vol} = (\lambda + 2\mu/3) \mathbf{P}^T \hat{\mathbf{P}}. \quad (101)$$

We note again, that in contrast to the symmetric Bézier \bar{B} method, the assembly of the stiffness matrix in this case can be performed in the standard way with no need for global matrix operations.

6.3 Numerical results

We begin this section by numerically evaluating the inf-sup constant for the global \bar{B} and non-symmetric Bézier \bar{B} methods. We then investigate the performance of the Bézier \bar{B} method for two nearly incompressible linear elasticity problems under plane strain conditions. For the numerical examples, we first study the Cook's membrane problem, which is discretized with B-spline basis functions, and in the second problem we model an infinite plate with a circular hole using NURBS. Results computed using standard finite elements are labeled Q_1 , Q_2 , Q_3 , and Q_4 . Results computed using a global \bar{B} method are labeled \mathcal{T}^{L^2} and those computed with the symmetric Bézier \bar{B} method and the non-symmetric Bézier \bar{B} method are labeled $S - \mathcal{T}^P$ and $NS - \mathcal{T}^P$, respectively.

6.3.1 Numerical evaluation of the inf-sup condition

The inf-sup condition is also referred to as the Ladyzhenskaya-Babuska-Brezzi condition (or simply LBB) [46–48]. It is a crucial condition to ensure the solvability, stability and optimality of a mixed problem. For the nearly incompressible elasticity problem the inf-sup condition is stated as: for $\delta p \neq 0$ and $\mathbf{u} \neq 0$

$$\inf_{\delta p \in L^2(\Omega)} \sup_{\mathbf{u} \in \mathcal{S}(\Omega)} \frac{|b(\mathbf{u}, \delta p)|}{\|\delta p\|_{L^2(\Omega)} \|\mathbf{u}\|_{H^1(\Omega)}} \geq \beta > 0. \quad (102)$$

In a discretized problem, the inf-sup condition requires the variable β to be a constant that is independent of the mesh size.

Here, we consider the inf-sup condition of a uniformly refined quarter annulus. The geometry and boundary conditions are shown in Figure 11. The geometry of the quarter annulus can be exactly represented using a biquadratic NURBS basis. The knot vector for the coarsest discretization is given by

$$\Xi_\xi \times \Xi_\eta = \{0, 0, 0, 1, 1, 1\} \times \{0, 0, 0, 1, 1, 1\} \quad (103)$$

and the corresponding weights and control points associated with each basis function are given in Table 1 and 2. For higher-order elements and finer discretizations the weights and corresponding control points are identified by an order elevation and knot insertion algorithm, respectively. The Bézier mesh representation for the discretizations are shown in Figure 12.

Only the global \bar{B} method and the non-symmetric Bézier \bar{B} method are considered here, as the symmetric Bézier \bar{B} method lacks a connection to a mixed formulation. As a counter example, the well-known pair Q_p/Q_p

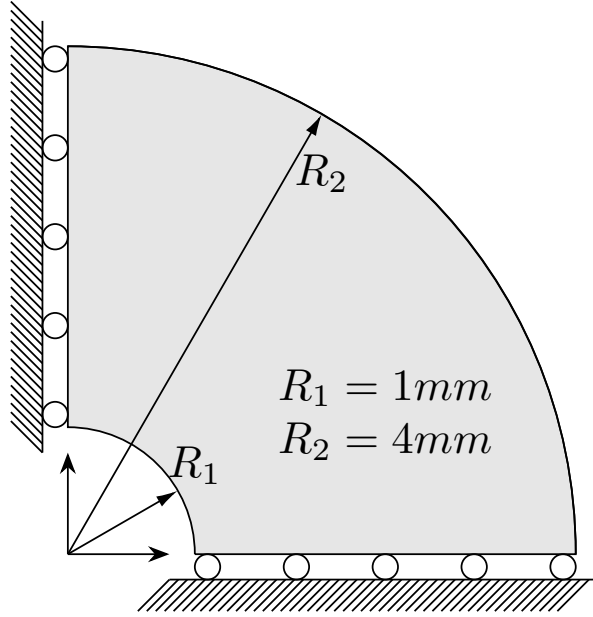


Figure 11: Geometry and boundary conditions for the inf-sup test.

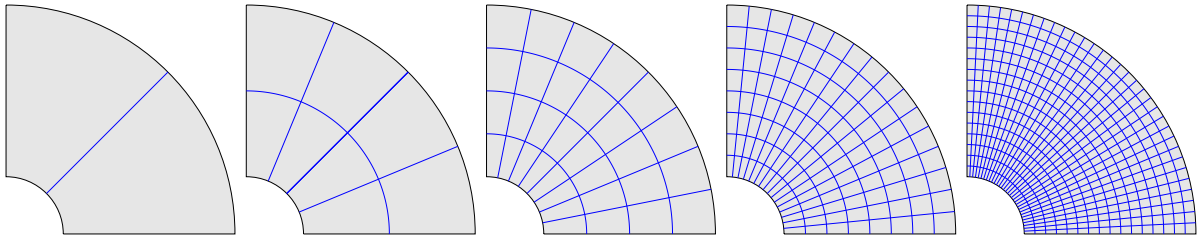


Figure 12: Sequence of meshes for inf-sup test.

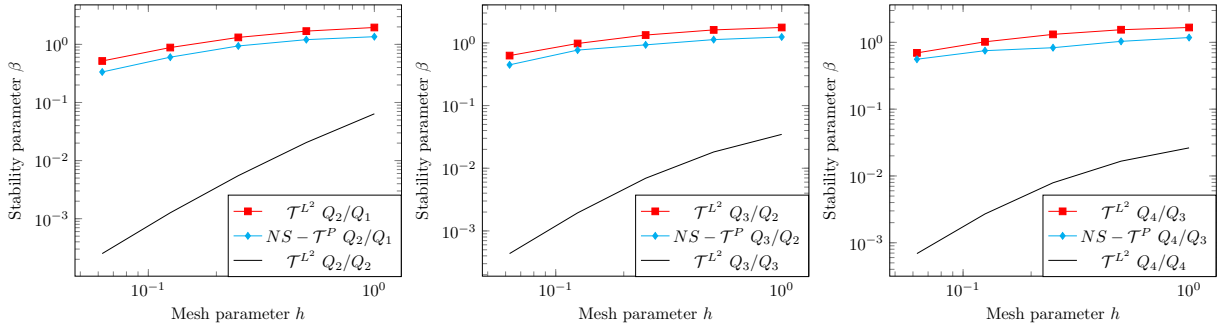


Figure 13: Inf-sup test results for nearly incompressible elasticity. The global \bar{B} method, $\mathcal{T}^{L^2} Q4/Q3$, and the non-symmetric Bézier \bar{B} method, $NS - \mathcal{T}^P Q4/Q3$, do not strictly satisfy the LBB condition, but compared to the $\mathcal{T}^{L^2} Q4/Q4$ method, both methods reduce constraints to a favorable level.

of the global \bar{B} method that violates the inf-sup condition is also tested here. Our tests follow the procedure proposed by Chapelle and Bathe in [49].

Figure 13 shows the numerical results. As can be seen, the global \bar{B} method and the non-symmetric Bézier \bar{B} method do not strictly satisfy the LBB condition since β is not independent of the mesh size. This result is consistent with the statement made in [40] that the global \bar{B} method does not reduce the constraints sufficiently to satisfy the LBB condition. However, compared to the Q_p/Q_p pair, both methods reduce constraints to a more favorable level. If we compare the results for the global \bar{B} method with the non-symmetric Bézier \bar{B} method we see that their stability parameter β decreases at the same rate and the stability parameter for the non-symmetric Bézier \bar{B} method is slightly lower than that for the global \bar{B} method. These results indicate a similar optimality in convergence for both methods and a slightly higher error for the non-symmetric Bézier \bar{B} method.

6.3.2 Cook's membrane problem

This benchmark problem is a standard test for combined bending and shearing response. The geometry, boundary conditions, and material properties are shown in Figure 14. The left boundary of the tapered panel is clamped, the top and bottom edges are free with zero traction boundary conditions, and the right boundary is subjected to a uniformly distributed traction load in the y -direction as shown. The meshes used are shown in Figure 15.

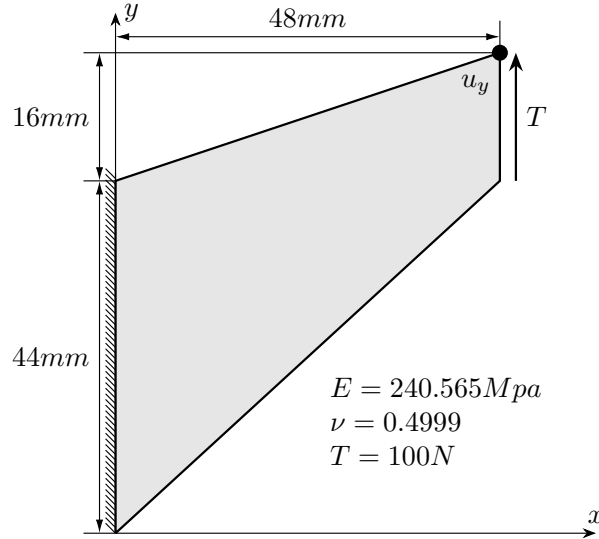


Figure 14: Geometry, boundary conditions, and material properties for the Cook's membrane problem.

A comparison of the displacement of the top right corner with respect to the number of elements per side is shown in Figure 16. Q_1 locks and mesh refinement has little impact. Locking is somewhat reduced for the higher-order elements Q_p , $p > 1$. The \bar{B} methods perform very well for all degrees.

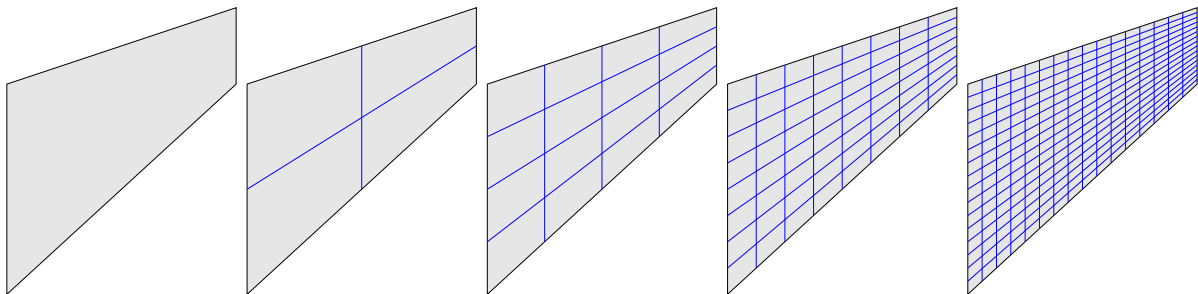
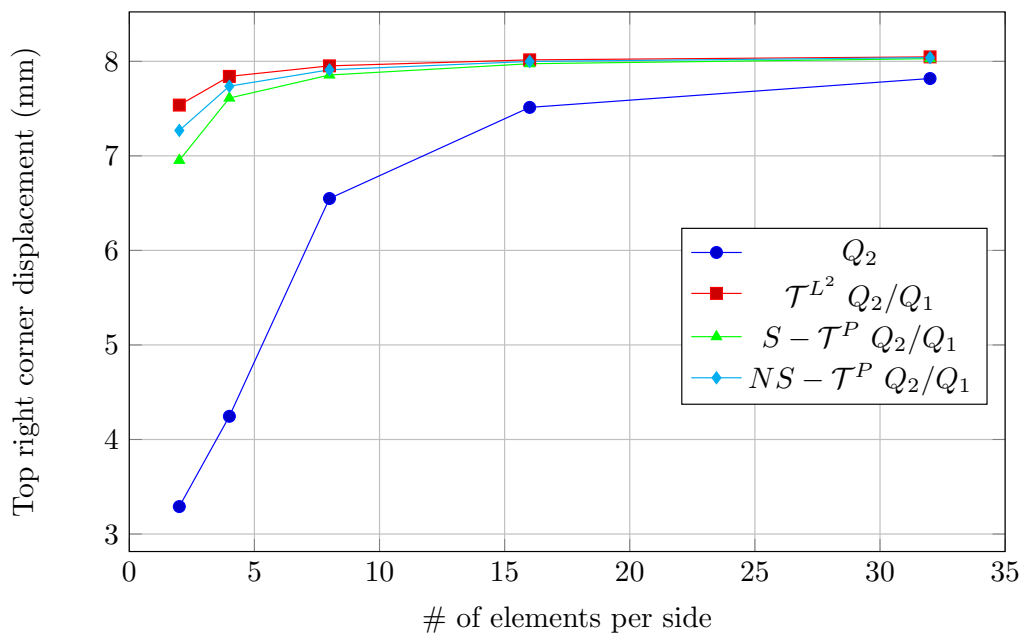
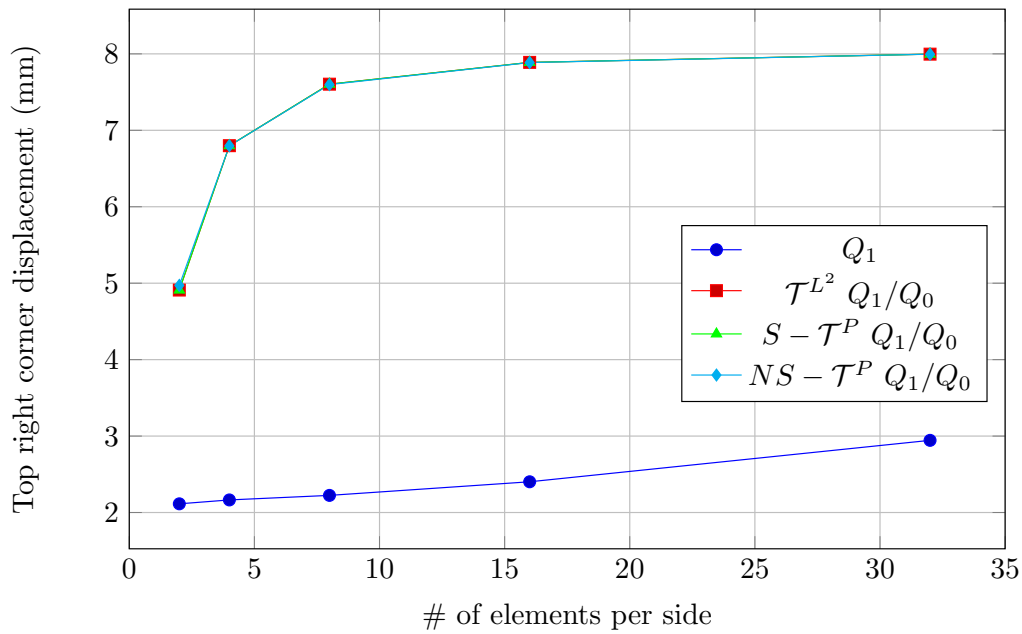


Figure 15: Sequence of meshes for Cook's membrane problem.



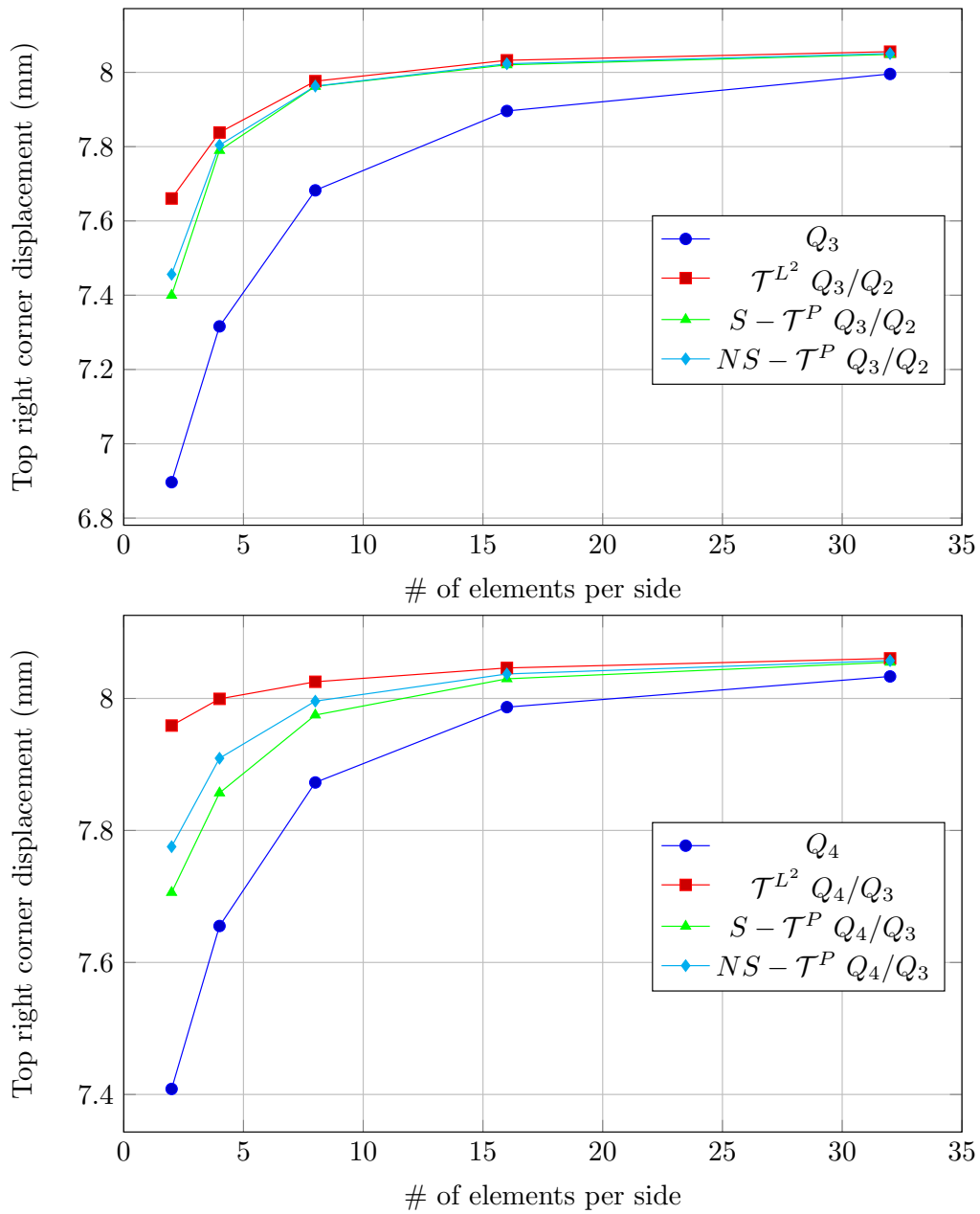
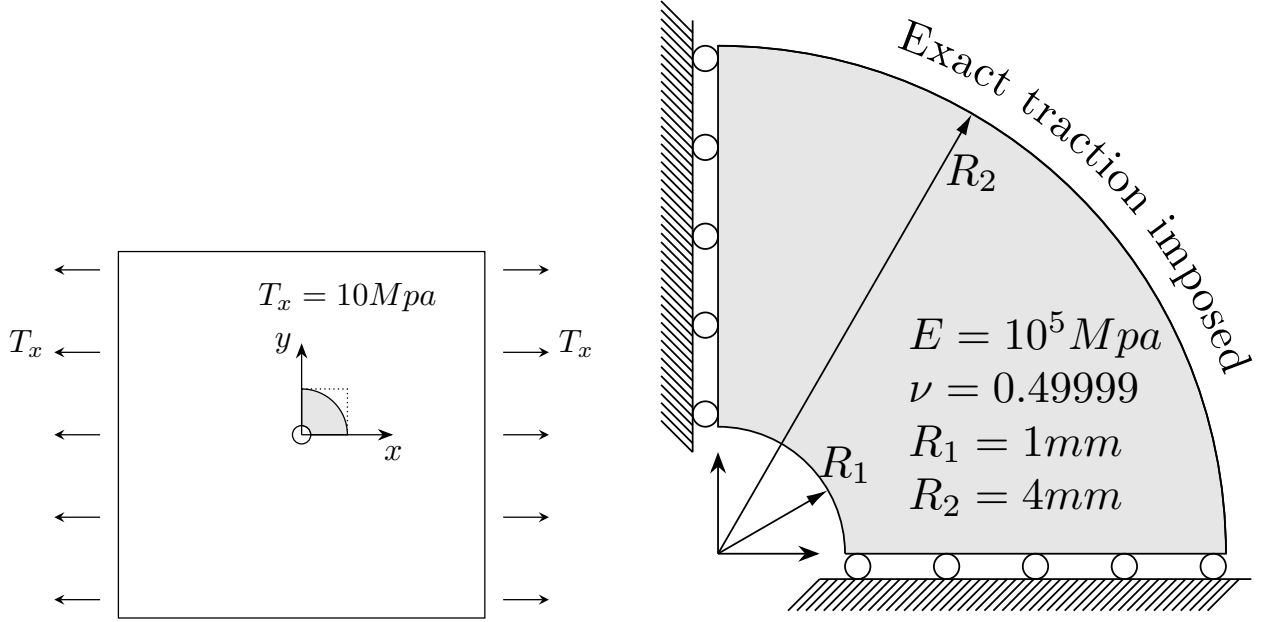


Figure 16: Cook's membrane: comparison of the vertical displacement at the top right corner for the different methods and degrees.

6.3.3 Infinite plate with a circular hole

The setup for the infinite plate with a circular hole problem is shown in Figure 17 and the discretizations are shown in Figure 12. The traction along the outer edge is evaluated from the exact solution which is given by

$$\begin{aligned}\sigma_{rr}(r, \theta) &= \frac{T_x}{2} \left(1 - \frac{R_1^2}{r^2}\right) + \frac{T_x}{2} \left(1 - 4\frac{R_1^2}{r^2} + 3\frac{R_1^4}{r^4}\right) \cos(2\theta) \\ \sigma_{\theta\theta}(r, \theta) &= \frac{T_x}{2} \left(1 + \frac{R_1^2}{r^2}\right) - \frac{T_x}{2} \left(1 + 3\frac{R_1^4}{r^4}\right) \cos(2\theta) \\ \sigma_{r\theta}(r, \theta) &= -\frac{T_x}{2} \left(1 + 2\frac{R_1^2}{r^2} - 3\frac{R_1^4}{r^4}\right) \sin(2\theta).\end{aligned}\tag{104}$$



(a) Infinite plate with a hole subjected to uniaxial tension at $x = \pm\infty$.

(b) A representation of the computational model.

Figure 17: Geometry, boundary conditions, and material properties for the infinite plate with a hole.

Convergence plots for the relative error of the displacement and energy in the L^2 norm are shown in Figure 18. As can be seen, the standard Q_p approximations suffer from severe volumetric locking for all orders while, on the other hand, the \bar{B} methods remedy locking for all cases. For the symmetric Bézier \bar{B} method, optimal rates are achieved in all three measures for biquadratic elements and the optimal energy convergence has been achieved for bicubic elements, but convergence has degraded in all three measures for the biquartic elements. This reduction in convergence rates results from the fact that the derivation of the symmetric Bézier \bar{B} method is purely based on the engineering analogy between the L^2 projection and Bézier projection operations. The non-symmetric Bézier \bar{B} method, on the other hand, achieves optimal convergence in the displacement, stress, and energy norms for all elements with slightly higher errors than those of the global \bar{B} method.

Contour plots of σ_{xx} from the finest biquartic discretization are shown in Figure 19. We can see that results from all \bar{B} methods are consistent with the reference solution, but using the standard finite element approach results in meaningless stresses. Figure 20 shows the absolute error of σ_{xx} from the same discretization. We can see that the projection methods produce an error of less than .1% of the maximum σ_{xx} , while the error for the standard Q_4 element is of the same order as the maximum σ_{xx} . We can also see that the non-symmetric method provides a slight improvement when compared to the symmetric method.

7 Conclusions

We have presented two Bézier \bar{B} projection methods, which we have called symmetric and non-symmetric Bézier \bar{B} projection, as an approach to overcome locking phenomena in structural mechanics applications of isogeometric analysis. Each approach maintains the sparsity of the resulting linear system. The methods

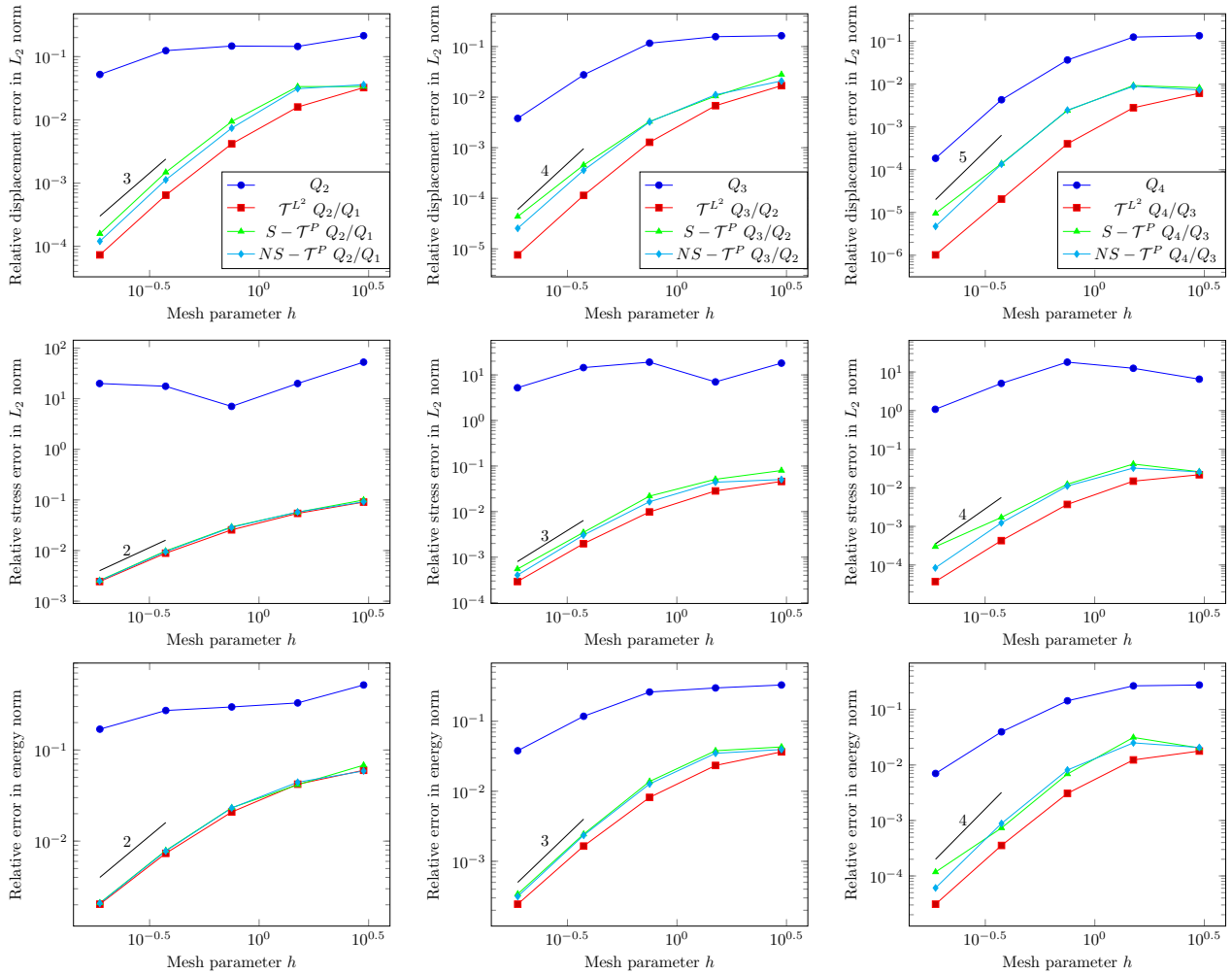


Figure 18: Convergence study of the plate with a circular hole. The relative L^2 error of displacement, stress and the relative error in energy norm with respect to mesh refinement.

utilize Bézier extraction and projection, which makes it simple to implement them in an existing finite element framework and makes it applicable to any spline representation which can be written in Bézier form. In contrast to global \bar{B} methods, which produce dense stiffness matrices, the Bézier \bar{B} approach results in a sparse stiffness matrix while still benefiting from higher-order convergence rates. We have made the connection between the non-symmetric method and a mixed formulation and shown that, although this method does not strictly satisfy the inf-sup condition, it reduces constraints sufficiently to provide optimal convergence rates for the problems studied here.

We have demonstrated the performance of the approach in the context of shear deformable beams (to alleviate transverse shear locking) and nearly incompressible elasticity problems (to alleviate volumetric locking). The proposed method reduces locking errors and achieves nearly optimal convergence rates for the symmetric method and optimal rates for the non-symmetric method. The cases where optimal rates were not achieved when using the the symmetric formulation are a symptom of the fact that the symmetric formulation is not directly related to a variational principle.

The two methods presented here provide a choice between a formulation that results in a symmetric stiffness matrix but requires matrix operations at the global level and potentially less accuracy and a formulation that results in a non-symmetric stiffness matrix that can be assembled in the standard element routine approach and achieves optimal convergence rates. The trade-offs are between higher costs in assembly for the symmetric formulation versus potentially higher costs in solving a non-symmetric system. In either case, however, the cost is less than using the standard \bar{B} formulation.

References

- [1] T. J. R. Hughes, J. A. Cottrell, Y. Bazilevs, Isogeometric analysis: CAD, finite elements, NURBS, exact geometry and mesh refinement, *Computer Methods in Applied Mechanics and Engineering* 194 (39) (2005)

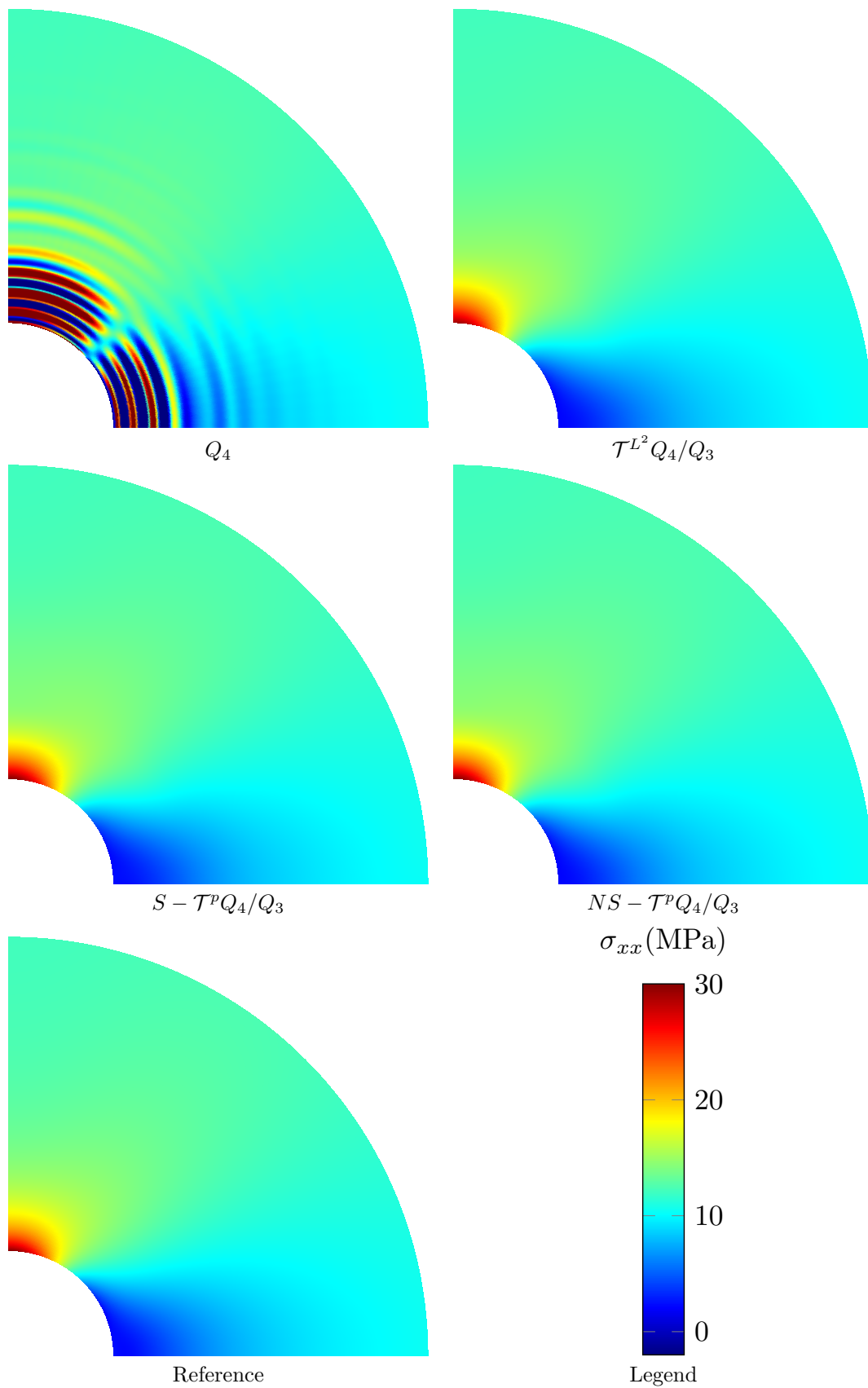


Figure 19: Contour plots of σ_{xx}^h for the plate with a circular hole ($p = 4$, and the finest mesh is used). For reference the analytical solution is also plotted.

4135–4195.

[2] J. A. Cottrell, T. J. R. Hughes, Y. Bazilevs, Isogeometric Analysis: Toward Integration of CAD and FEA,

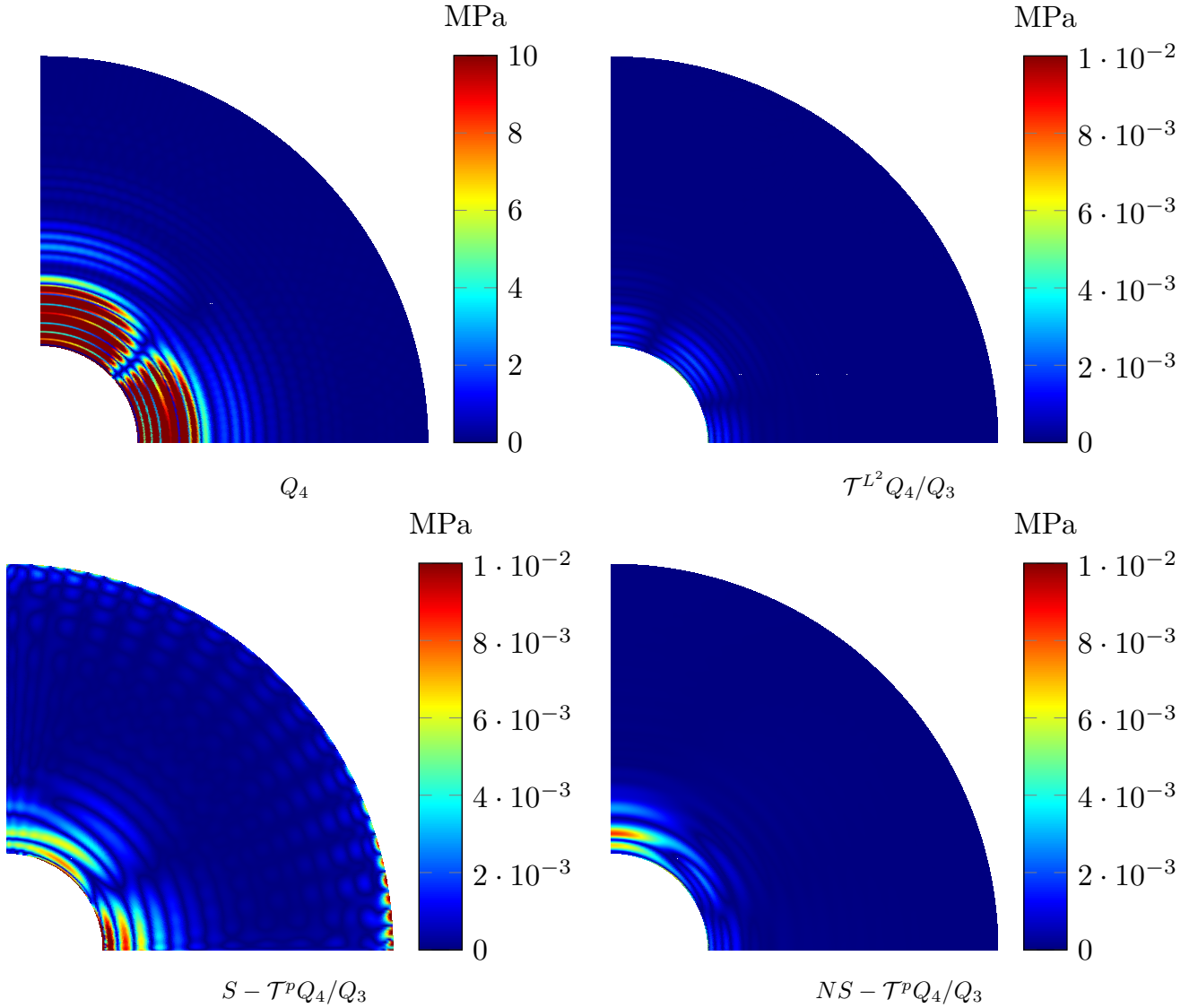


Figure 20: Contour plots of $|\sigma_{xx} - \sigma_{xx}^h|$ for the plate with a circular hole ($p = 4$, and the finest mesh is used).

John Wiley & Sons, 2009.

- [3] J. A. Cottrell, T. J. R. Hughes, A. Reali, Studies of refinement and continuity in isogeometric structural analysis, *Computer Methods in Applied Mechanics and Engineering* 196 (41) (2007) 4160–4183.
- [4] J. A. Cottrell, A. Reali, Y. Bazilevs, T. J. R. Hughes, Isogeometric analysis of structural vibrations, *Computer Methods in Applied Mechanics and Engineering* 195 (41) (2006) 5257–5296.
- [5] T. J. R. Hughes, A. Reali, G. Sangalli, Duality and unified analysis of discrete approximations in structural dynamics and wave propagation: Comparison of p-method finite elements with k-method NURBS, *Computer Methods in Applied Mechanics and Engineering* 197 (49) (2008) 4104–4124.
- [6] Y. Bazilevs, V. M. Calo, J. A. Cottrell, J. A. Evans, T. J. R. Hughes, S. Lipton, M. A. Scott, T. W. Sederberg, Isogeometric analysis using T-splines, *Computer Methods in Applied Mechanics and Engineering* 199 (5) (2010) 229–263.
- [7] J. A. Evans, Y. Bazilevs, I. Babuška, T. J. R. Hughes, n-widths, sup-infs, and optimality ratios for the k-version of the isogeometric finite element method, *Computer Methods in Applied Mechanics and Engineering* 198 (21) (2009) 1726–1741.
- [8] T. W. Sederberg, J. Zheng, A. Bakenov, A. Nasri, T-splines and T-NURCCs, in: *ACM SIGGRAPH 2003 Papers, SIGGRAPH '03*, ACM, 2003, pp. 477–484.
- [9] M. A. Scott, X. Li, T. W. Sederberg, T. J. R. Hughes, Local refinement of analysis-suitable T-splines, *Computer Methods in Applied Mechanics and Engineering* 213 (2012) 206–222.

- [10] X. Li, M. A. Scott, Analysis-suitable T-splines: Characterization, refineability, and approximation, *Mathematical Models and Methods in Applied Sciences* 24 (6) (2013) 1141–1164.
- [11] P. B. Bornemann, F. Cirak, A subdivision-based implementation of the hierarchical b-spline finite element method, *Computer Methods in Applied Mechanics and Engineering* 253 (2013) 584–598.
- [12] M. A. Scott, D. C. Thomas, E. J. Evans, Isogeometric spline forests, *Computer Methods in Applied Mechanics and Engineering* 269 (2014) 222–264.
- [13] D. Schillinger, L. Dedè, M. A. Scott, J. A. Evans, M. J. Borden, E. Rank, T. J. R. Hughes, An isogeometric design-through-analysis methodology based on adaptive hierarchical refinement of NURBS, immersed boundary methods, and T-spline CAD surfaces, *Computer Methods in Applied Mechanics and Engineering* 249 (2012) 116–150.
- [14] E. J. Evans, M. A. Scott, X. Li, D. C. Thomas, Hierarchical T-splines: Analysis-suitability, Bézier extraction, and application as an adaptive basis for isogeometric analysis, *Computer Methods in Applied Mechanics and Engineering* 284 (2015) 1–20.
- [15] D. R. Forsey, R. H. Bartels, Hierarchical b-spline refinement, in: *Proceedings of the 15th Annual Conference on Computer Graphics and Interactive Techniques, SIGGRAPH '88*, ACM, 1988, pp. 205–212.
- [16] T. Dokken, T. Lyche, K. F. Pettersen, Polynomial splines over locally refined box-partitions, *Computer Aided Geometric Design* 30 (3) (2013) 331–356.
- [17] K. A. Johannessen, T. Kvamsdal, T. Dokken, Isogeometric analysis using LR b-splines, *Computer Methods in Applied Mechanics and Engineering* 269 (2014) 471–514.
- [18] D. C. Thomas, M. A. Scott, J. A. Evans, K. Tew, E. J. Evans, Bézier projection: A unified approach for local projection and quadrature-free refinement and coarsening of NURBS and T-splines with particular application to isogeometric design and analysis, *Computer Methods in Applied Mechanics and Engineering* 284 (2015) 55–105.
- [19] M. J. Borden, M. A. Scott, J. A. Evans, T. J. R. Hughes, Isogeometric finite element data structures based on Bézier extraction of NURBS, *International Journal for Numerical Methods in Engineering* 87 (1) (2011) 15–47.
- [20] M. A. Scott, M. J. Borden, C. V. Verhoosel, T. W. Sederberg, T. J. R. Hughes, Isogeometric finite element data structures based on Bézier extraction of T-splines, *International Journal for Numerical Methods in Engineering* 88 (2) (2011) 126–156.
- [21] D. S. Malkus, T. J. R. Hughes, Mixed finite element methods — Reduced and selective integration techniques: A unification of concepts, *Computer Methods in Applied Mechanics and Engineering* 15 (1) (1978) 63–81.
- [22] O. C. Zienkiewicz, R. L. Taylor, J. M. Too, Reduced integration technique in general analysis of plates and shells, *International Journal for Numerical Methods in Engineering* 3 (2) (1971) 275–290.
- [23] J. C. Nagtegaal, D. M. Parks, J. R. Rice, On numerically accurate finite element solutions in the fully plastic range, *Computer Methods in Applied Mechanics and Engineering* 4 (2) (1974) 153–177.
- [24] T. J. R. Hughes, Generalization of selective integration procedures to anisotropic and nonlinear media, *International Journal for Numerical Methods in Engineering* 15 (9) (1980) 1413–1418.
- [25] R. P. R. Cardoso, J. M. A. Cesar de Sa, The enhanced assumed strain method for the isogeometric analysis of nearly incompressible deformation of solids, *International Journal for Numerical Methods in Engineering* 92 (1) (2012) 56–78.
- [26] J. Dolbow, T. Belytschko, Volumetric locking in the element free Galerkin method, *International Journal for Numerical Methods in Engineering* 46 (6) (1999) 925–942.
- [27] E. P. Kasper, R. L. Taylor, A mixed-enhanced strain method: Part I: Geometrically linear problems, *Computers & Structures* 75 (3) (2000) 237–250.
- [28] T. Hughes, On the variational foundations of assumed strain methods, *Journal of applied mechanics* 53 (1986) 51.
- [29] R. L. Taylor, Isogeometric analysis of nearly incompressible solids, *International Journal for Numerical Methods in Engineering* 87 (1-5) (2011) 273–288.

- [30] R. Echter, M. Bischoff, Numerical efficiency, locking and unlocking of NURBS finite elements, *Computer Methods in Applied Mechanics and Engineering* 199 (5) (2010) 374–382.
- [31] R. Bouclier, T. Elguedj, A. Combescure, Locking free isogeometric formulations of curved thick beams, *Computer Methods in Applied Mechanics and Engineering* 245 (2012) 144–162.
- [32] J. Kiendl, K. U. Bletzinger, J. Linhard, R. Wüchner, Isogeometric shell analysis with Kirchhoff–Love elements, *Computer Methods in Applied Mechanics and Engineering* 198 (49) (2009) 3902–3914.
- [33] J. Kiendl, M. C. Hsu, M. Wu, A. Reali, Isogeometric Kirchhoff–Love shell formulations for general hyper-elastic materials, *Computer Methods in Applied Mechanics and Engineering* 291 (2015) 280–303.
- [34] B. Oesterle, R. Sachse, E. Ramm, M. Bischoff, Hierarchic isogeometric large rotation shell elements including linearized transverse shear parametrization, *Computer Methods in Applied Mechanics and Engineering* 321 (2017) 383–405.
- [35] B. Oesterle, E. Ramm, M. Bischoff, A shear deformable, rotation-free isogeometric shell formulation, *Computer Methods in Applied Mechanics and Engineering* 307 (2016) 235–255.
- [36] R. Echter, B. Oesterle, M. Bischoff, A hierarchic family of isogeometric shell finite elements, *Computer Methods in Applied Mechanics and Engineering* 254 (2013) 170–180.
- [37] C. Adam, S. Bouabdallah, M. Zarroug, H. Maitournam, Improved numerical integration for locking treatment in isogeometric structural elements, Part I: Beams, *Computer Methods in Applied Mechanics and Engineering* 279 (2014) 1–28.
- [38] C. Adam, S. Bouabdallah, M. Zarroug, H. Maitournam, Improved numerical integration for locking treatment in isogeometric structural elements. Part II: Plates and shells, *Computer Methods in Applied Mechanics and Engineering* 284 (2015) 106–137.
- [39] C. Adam, T. J. R. Hughes, S. Bouabdallah, M. Zarroug, H. Maitournam, Selective and reduced numerical integrations for NURBS-based isogeometric analysis, *Computer Methods in Applied Mechanics and Engineering* 284 (2015) 732–761.
- [40] T. Elguedj, Y. Bazilevs, V. M. Calo, T. J. Hughes, B-bar and F-bar projection methods for nearly incompressible linear and non-linear elasticity and plasticity using higher-order NURBS elements, *Computer Methods in Applied Mechanics and Engineering* 197 (33-40) (2008) 2732–2762.
- [41] R. Bouclier, T. Elguedj, A. Combescure, Efficient isogeometric nurbs-based solid-shell elements: Mixed formulation and \bar{B} -method, *Computer Methods in Applied Mechanics and Engineering* 267 (2013) 86–110.
- [42] T. J. Mitchell, S. Govindjee, R. L. Taylor, A method for enforcement of Dirichlet boundary conditions in isogeometric analysis, *Recent Developments and Innovative Applications in Computational Mechanics* (2011) 283–293.
- [43] S. Govindjee, J. Strain, T. J. Mitchell, R. L. Taylor, Convergence of an efficient local least-squares fitting method for bases with compact support, *Computer Methods in Applied Mechanics and Engineering* 213 (2012) 84–92.
- [44] T. J. R. Hughes, *The finite element method: Linear static and dynamic finite element analysis*, Dover, 2000.
- [45] J. Kiendl, F. Auricchio, T. J. R. Hughes, A. Reali, Single-variable formulations and isogeometric discretizations for shear deformable beams, *Computer Methods in Applied Mechanics and Engineering* 284 (2015) 988–1004.
- [46] I. Babuška, The finite element method with lagrangian multipliers, *Numerische Mathematik* 20 (3) (1973) 179–192.
- [47] F. Brezzi, On the existence, uniqueness and approximation of saddle-point problems arising from lagrangian multipliers, *Revue française d’automatique, informatique, recherche opérationnelle. Analyse numérique* 8 (R2) (1974) 129–151.
- [48] O. A. Ladyzhenskaya, *The mathematical theory of viscous incompressible flow*, Vol. 12, Gordon & Breach New York, 1969.
- [49] D. Chapelle, K. J. Bathe, The inf-sup test, *Computers & Structures* 47 (4) (1993) 537 – 545.